Insights on fault reactivation during the 2019 November 11, Mw 4.9 Le Teil earthquake in southeastern France, from a joint 3-D geological model and InSAR time-series analysis

L. Marconato, P. H. Leloup, C. Lasserre, R. Jolivet, Séverine Caritg, R. Grandin, M. Métois, O. Cavalié, L. Audin

Geophysical Journal International

Geophys. J. Int. (2022) **229,** 758–775
Advance Access publication 2021 December 11
GJI Seismology

https://doi.org/10.1093/gji/ggab498

Insights on fault reactivation during the 2019 November 11, M_w 4.9 Le Teil earthquake in southeastern France, from a joint 3-D geological model and InSAR time-series analysis

L. Marconato [1], P. H. Leloup,[1] C. Lasserre [1], R. Jolivet,[2,3] S. Caritg,[4] R. Grandin [5], M. Métois,[1] O. Cavalié[1,6] and L. Audin[7]

[1] *Univ Lyon, Univ Lyon* 1, *ENSL, CNRS, LGL-TPE, F-*69622 *Villeurbanne, France. E-mail: leo.marconato@ens-lyon.fr*
[2] *Laboratoire de Géologie, Département de Géosciences, École Normale Supérieure, PSL Université, CNRS UMR* 8538, *Paris, France*
[3] *Institut Universitaire de France,* 1 *rue Descartes,* 75006 *Paris, France*
[4] *Bureau de Recherches Géologiques et Minières (BRGM), France*
[5] *Institut de Physique du globe de Paris, CNRS, Université de Paris, F-*75005 *Paris, France*
[6] *Observatoire de la Côte d'Azur, Université Côte d'Azur, IRD, CNRS, Géoazur, France*
[7] *ISTerre, Univ. Grenoble Alpes, CNRS, IRD, Grenoble, France*

Accepted 2021 December 9. Received 2021 October 27; in original form 2021 May 28

SUMMARY

The 2019, M_w 4.9 Le Teil earthquake occurred in southeastern France, causing substantial damage in this slow deforming region. Field observations, remote sensing and seismological studies following the event revealed that coseismic slip concentrates at shallow depth along a ∼5 km long rupture associated with surface breaks and a thrusting mechanism. We further investigate this earthquake by combining geological field mapping, 3-D geology, InSAR time-series analysis and a coseismic slip inversion. From structural, stratigraphic and geological data collected around the epicentre, we first produce a 3-D geological model of the region surrounding the rupture using the GeoModeller software. Our model includes the geometry of the geological layers and the main faults, including the La Rouvière Fault, (LRF) the Oligocene normal fault that ruptured during the earthquake. We generate a time-series of surface displacement from Sentinel-1 SAR data ranging from early 2019 January to late 2020 January using the NSBAS processing chain. The spatio-temporal patterns of surface displacement for this time span show neither a clear pre-seismic signal nor significant post-seismic transient deformation. We extract the coseismic displacement pattern from the InSAR time-series, highlighting along-strike variations of coseismic surface slip. The maximum relative displacement along the line of sight is up to ∼16 cm and is located in the southwestern part of the rupture. We invert for the slip distribution on the fault from the InSAR coseismic surface displacement field. Constraining our fault geometry from the geological model, acceptable fault dip ranges between 55° and 60°. Our model confirms the reactivation of LRF, with reverse slip at very shallow depth and two main slip patches reaching, respectively, 30 and 24 cm of slip, both around 500 m depth. We finally discuss how the 3-D fault geometry and geological structure may have impacted the slip distribution and propagation during the earthquake. This study is a step to reassess the seismic hazard of the many faults similar to the La Rouvière one along the Cévennes fault system, in a densely populated area hosting several sensitive nuclear sites.

Key words: Radar interferometry; Seismic cycle; Inverse theory; Time-series analysis; Earthquake source observations; Continental neotectonics.

1 INTRODUCTION

On 2019 November 11, the M_w 4.9 Le Teil earthquake struck the region of Montélimar, in the western Rhône valley in South-East France (Fig. 1a). The towns of Le Teil, Saint-Thomé and Viviers, all located in the epicentral area, suffered important economic damages (∼50M€). Thankfully, only a small number of injured people were reported. Partial building collapse happened in a radius of about 10 km corresponding to macroseismic intensities of VII–VIII (EMS98; Cornou *et al*. 2021). The earthquake caused the temporary

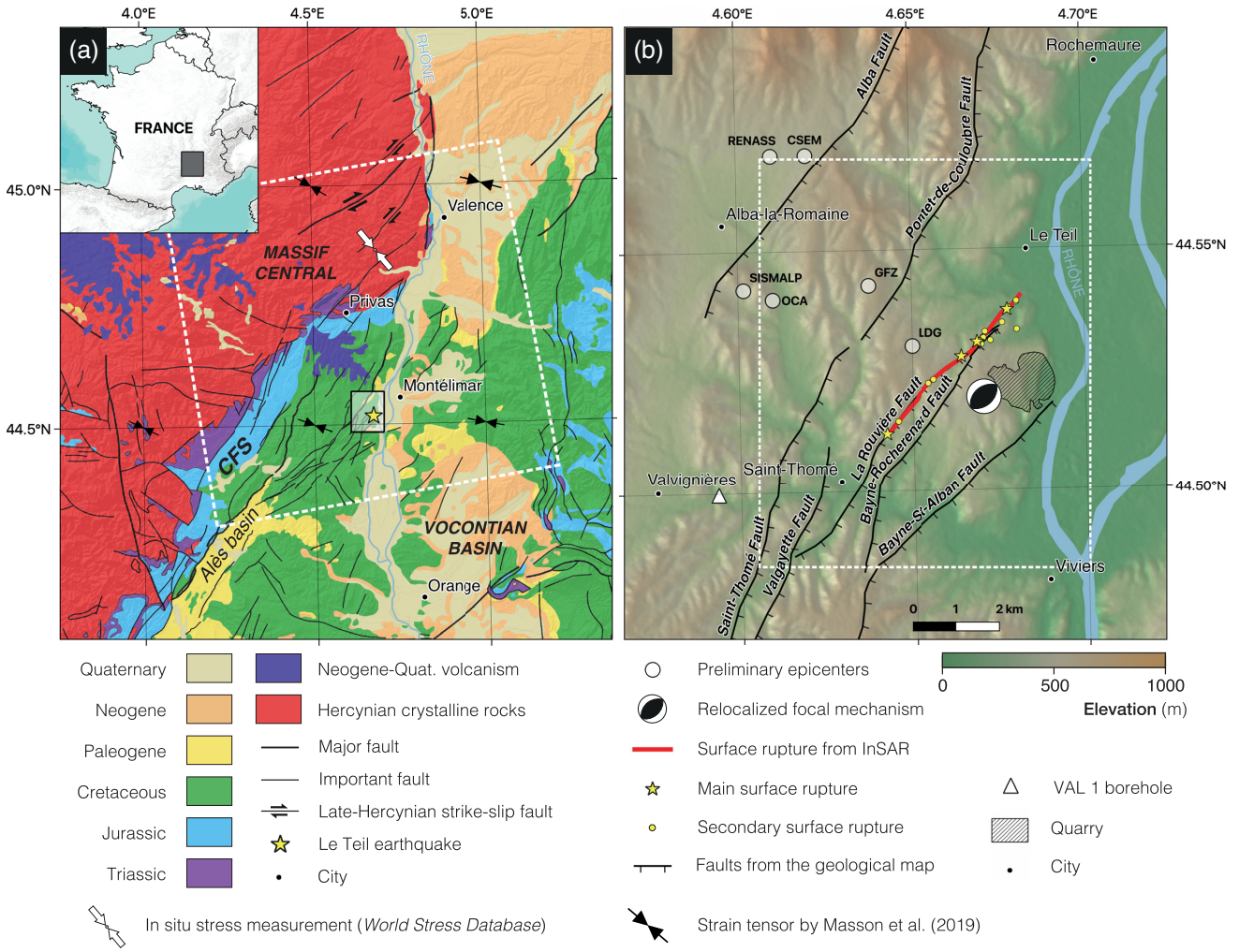

Figure 1. Geological and seismotectonic setting of the Le Teil earthquake. (a) Regional geological and structural map (Chantraine *et al*. 1996). Black arrows show the principal horizontal compressive directions of the strain tensor (Masson *et al*. 2019). White dashed outline shows coverage of reprocessed InSAR data. (b) Surface rupture trace is in red. Yellow dots indicating location of field observations of coseismic displacement from Ritz *et al*. (2020). Faults in black are from Saint Martin (2009). Rectangle in dotted white in panel (b) show coverage of the 3-D geological model in Fig. 2. Revised location of epicentre (yellow star in a) and focal mechanism are from Delouis *et al*. (2021).

shutdown of a nuclear power plant located 15 km to the north of the epicentre for security check.

The first epicentral localizations obtained by seismological institutes all being inaccurate by several kilometres (Fig. 1b), it is the first Sentinel-1 interferograms that allowed a precise localization of the Le Teil earthquake (Cornou *et al*. 2021). These interferograms show a sharp surface rupture (Ritz *et al*. 2020) suggesting that the earthquake ruptured the La Rouvière Fault (LRF), a normal fault previously mapped (Kerrien *et al*. 1989) and considered inactive since the Oligocene. The reverse-faulting and very shallow (< 3 km) focal mechanisms estimates matched InSAR imagery, suggesting a reactivation of the shallow part of the LRF in reverse motion, hence with an inversion of its kinematics. In addition, the strong mobilization of the French scientific community (Delouis *et al*. 2019; Cornou *et al*. 2021), guided by InSAR imagery, led to the identification of several surface breaks associated with the Le Teil event, matching both the preliminary trace inferred from InSAR data and the previously mapped trace of the LRF (Ritz *et al*. 2020, Fig. 1b). Up to 13 cm of surface displacement was measured on the field, and InSAR suggested up to 15 cm of relative surface motion.

The occurrence of such shallow reverse faulting earthquake along a previously thought to be inactive normal fault raises several issues. The reactivation of the LRF must be examined in the light of the geological context and the fault geometry. In addition, the potential triggering of the event by the surface unloading induced by excavation in a cement quarry located in the immediate vicinity of the LRF is still debated (Ampuero *et al*. 2020; De Novellis 2020). The hypothesis of excavation induced triggering is favoured by the very shallow depth of the event and the lack of aftershock (Delouis *et al*. 2019). The reassessment of the seismic hazard zoning must also be considered in the whole Ardèche margin where faults similar to the LRF are collocated with several nuclear facilities and populated areas.

From a more fundamental point of view, as fault geometry and geological, lithological and structural inheritance appear to be key factors to understand the extent and the variability of slip during earthquakes (e.g. King & Nabelek 1985; Wesnousky 2006; Choi *et al*. 2018), the Le Teil earthquake represents a rare opportunity to study the interaction between pre-existing geological 3-D structures and earthquake deformation in a slow deforming context. The very

shallow slip distribution of this rather small event allows to put together different geological and geodetic data sets at a resolution (hundreds of metres) at which larger earthquake ruptures can hardly be studied.

We investigate the Le Teil earthquake combining field mapping, 3-D structural and geological modelling, InSAR time-series analysis and inversion for coseismic slip distribution. First, from field mapping, we constrain the geological formations and faults around the epicentral area and produce a 3-D numerical model of the geological layers and faults, including the LRF. Then, we compute a one-year InSAR Sentinel-1 time-series, covering 10 months prior and three months after the earthquake, in order to both refine the spatial coverage of the coseismic displacement map in the near field and investigate whether pre-seismic deformation or afterslip may have occurred or not. We model the slip distribution using the surface deformation field of the Le Teil earthquake. We compare our slip distribution with the geological and morphological features of the area. This multidisciplinary approach provides constraints about the geometry of the LRF, opening the discussion on the potential factors that controlled the reactivation of the fault and on the need to reassess seismic hazard in this region.

2 GEOLOGICAL AND STRUCTURAL HISTORY OF Le TEIL AREA

The Le Teil earthquake occurred in the so-called Vivaro-Cévenole margin in between the Hercynian crystalline basement of the Massif Central to the NW, and the Vocontian Mesozoic basin to the SE (Fig. 1a). The margin between these two domains corresponds to a ∼900 m topographic change and a network of NE-SW faults that runs for more than 150 km from the Bas Dauphiné to the Languedoc. This fault network, called the Cévennes fault system (CFS), shows evidence for a long and polyphased structural history with compression, strike-slip and extension phases during the Palaeozoic, extension phases during the Mesozoic and extension and compression phases during the Cenozoic.

NW-SE faults with apparent dextral offset affect the basement but not the Mesozoic cover (Fig. 1a, e.g. Chantraine *et al*. 1996) and are interpreted as Late Hercynian strike-slip faults (Arthaud & Matte 1975; Chardon *et al*. 2020) that may have been reactivated during the later deformation phases. The end of the Hercynian orogenic cycle corresponds to a carboniferous phase of detrital sediments and coal deposit as well as several deformation phases. Widespread erosion was then followed by the deposit of Triassic continental sediments. During the Mesozoic more than 10 km of marine sediments accumulated in the Vocontian basin. At that time, the Vivaro-Cévenole margin corresponded to a network of NW-SE synsedimentary normal faults delimiting tilted blocks (Elmi 1983; 1996; Soechting 1996). The precise mode and direction of extension varied through time with three extension stages: Middle Triassic pre-rift, Early-Middle Jurassic Thethysian rifting and Late Jurassic-Early Cretaceous thermal subsidence (Elmi 1983; Bonijoly *et al*. 1996). From the interpretation of three seismic lines, a gravimetry map, and two deep boreholes located ∼25 km west of Le Teil (Fig. 1a), Bonijoly *et al*. (1996) propose a WNW-ESE balanced cross-section of the Vivaro-Cévenole margin. That section shows normal faults, mostly dipping to the SE, rooting on a SE dipping decollement within Carboniferous coal levels. Microstructural studies in the same area indicate a Triassic E-W extension (Bergerat & Martin 1993) and a Lower Jurassic N-S extension, while the main normal faults strike ∼N30 (Bergerat & Martin 1994; Martin & Bergerat 1996). At other locations along the Vivaro-Cévenole margin, the Lower Jurassic extension is considered to trend NW-SE, in better accordance with NE-SW striking normal faults (Blés *et al*. 1989 and references therein). The Lower Cretaceous corresponds to the widespread sedimentation of the so-called Urgonian carbonate platform in the Vocontian basin, in an N-S extension context (Blés *et al*. 1989, and references therein). Thermal modelling of Apatite fission track ages of samples from the Cévennes suggest that Mesozoic sedimentation extended further to the West than the present-day cover-basement boundary, but was eroded before the Upper Cretaceous (Barbarand *et al*. 2001; Gautheron *et al*. 2009).

Starting from the Aptian, sedimentation becomes detrital, probably because of local regression under far-field effects of the so-called Pyrenean N-S compression. At that time, the CFS was a left-lateral ramp bounding to the west the shortened cover with an ∼17 km offset of Upper Jurassic recifal facies in the south (Bodeur 1976). Associated NE-SW to N-S shortening occurred along several thrusts with decollements in the Triassic evaporites and Mesozoic marls (Arthaud & Seguret 1981; Arthaud & Laurent 1995).

At the end of the Eocene and during the Oligocene, rift basins straddle across western Europe from the North Sea to the Mediterranean Sea, contemporaneously with compression in the Western Alps, opening of the Golfe du Lion and volcanism in the Massif Central (Illies 1972; Bergerat 1987; Serane *et al*. 1995; Dèzes *et al*. 2004). At this time NW-SE extension prevails along the CFS, and several NE-SW normal faults are activated (Blés *et al*. 1989; Roure *et al*. 1992, and references therein). Some of the faults bound narrow rift basins filled with Oligocene deposits, the largest being the Alès basin (Fig. 1a) which is bounded by a major SE dipping fault (Arène *et al*. 1978). At the surface, the Alès fault dips 35° to the ESE but appears along seismic profiles as a ∼15° dipping fault at depth (Roure *et al*. 1992; Sanchis & Séranne 2000). The latest study considers that this fault has been active during a two stages extension history starting in the Eocene (Ludian) and connects with a decollement level in the Triassic (Sanchis & Séranne 2000). Further North, the CFS appears to splay out, with the Lagorce-Vallon, La-Fare-Pontet-de-Couloubre and Larnar-Bayne-St-Alban faults (Figs 1a and 2). Oligocene sediments were found in the hangingwall (at SE) of some of these faults at Ellieux (Larnas F.), Couijanet (Baynes-St-Alban F.) and Rochemaure (Pontet-de-Couloubre F.) (Figs 1a and 2; Kerrien *et al*. 1989), suggesting that the faults are Oligocene normal faults. From a balanced cross-section across that part of the margin, Roure *et al*. (1992; 1994, Fig. 1a) interpret the westernmost faults of the margin to be Lower Jurassic normal faults rooted in the Carboniferous, and the easternmost ones as Oligocene faults partly reactivating Lower Jurassic normal faults but rooted in the Triassic. The Bayne-St-Alban fault possibly connects with the Marsanne fault on the other side of the Rhône River that also separates Mesozoic from Oligocene sediments (Fig. 1a). The Pontet de Couloubre fault continues further NE and possibly connects with the Valence fault that bounds a thick Eocene-Oligocene half graben buried below Plio-quaternary and Miocene sediments (Deville *et al*. 1994; Kalifi *et al*. 2021). The Le Teil area is thus located in a relay zone between the N5 trending Valence and the N40 trending Alès Oligocene normal faults (Fig. 1a).

During the Miocene, continental and marine sedimentation takes place in the Rhodano-provençal flexural basin coevally with intense folding and thrusting at the front of the western Alps (Fig. 1a, Ford & Lickorish 2004). In the Le Teil area, the Oligocene sediments are affected, together with the underlying Mesozoic sediments, by

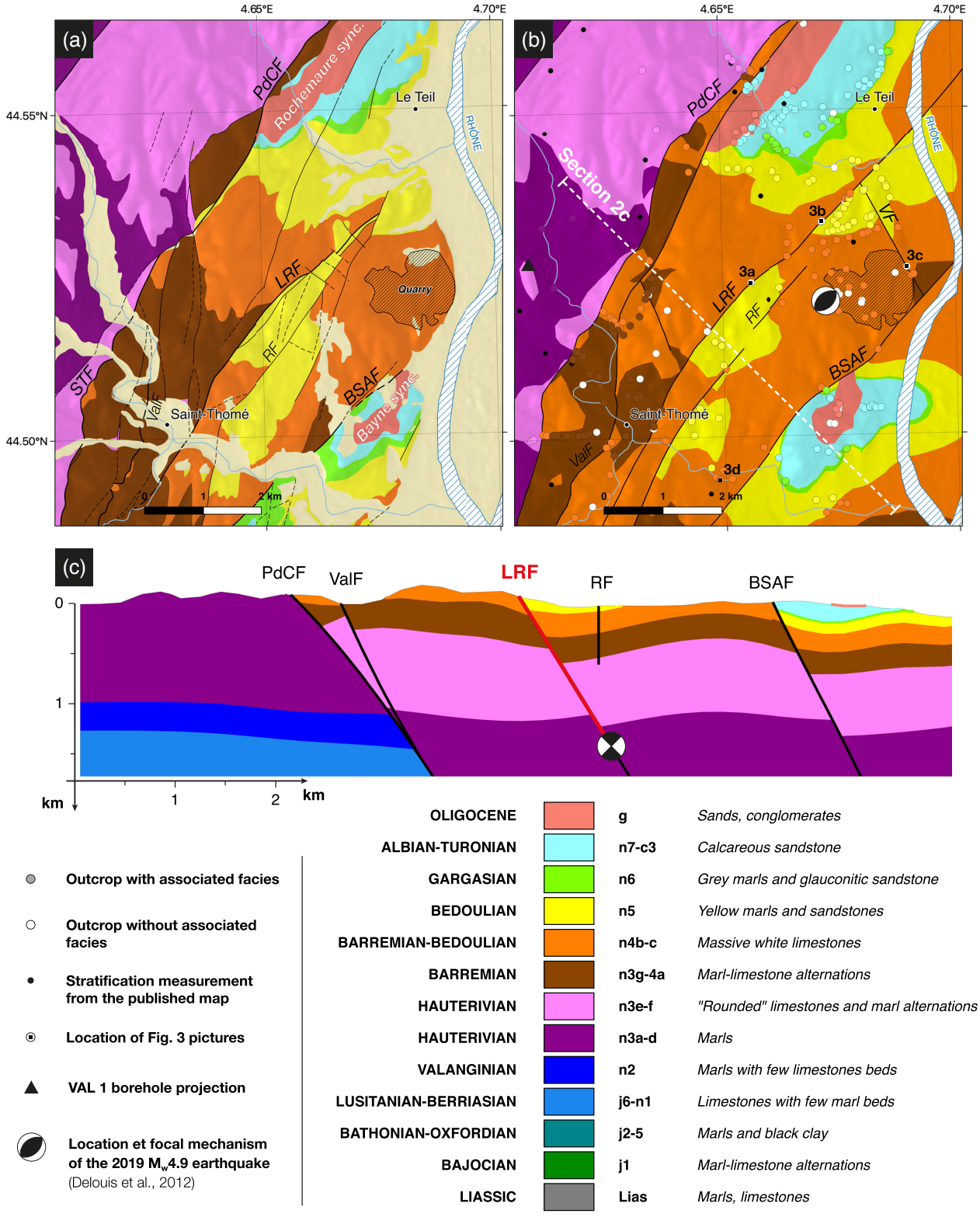

Figure 2. Geological maps and cross-section of the rupture area. (a) Ardèche Geological map (Saint Martin 2009) with original geological units grouped according to the 3-D model stratigraphic pile shown below (see Section 3.2 and Fig. S1, Supporting Information). Faults' names as defined by Elmi *et al.* (1996). (b) Surface map of the 3-D geological model. Coloured dots indicate location of surface observations used to constrain the 3-D model; circled dots labelled 3a to 3d show location of Fig. 3 pictures. The star shows location of the Le Teil earthquake epicentre (Delouis *et al.* 2021) (c) Geological cross-section across the 3-D model, along the trace shown in (b). The star shows the projected location of the Le Teil earthquake hypocenter (Delouis *et al.* 2021) and the red segment of the LRF represents the part that ruptured during the earthquake. *PdCF:* Pontet-de-Couloubre fault; *STF:* Saint-Thomé fault; *ValF:* Valgayette fault; *LRF:* La Rouvière fault; *RF:* Rocherenard fault; *VF:* Violette Fault; and *SAF:* Bayne-St-Alban fault.

NNE-SSW folds: the Rochemaure and Bayne synclines (Fig. 2), and the Serre des Parts and Vivier anticlines (Elmi *et al*. 1996). As this compression appears to be mostly visible in the eastern part of the zone, it was termed 'Rhodanian' and attributed to a Miocene compression (Elmi *et al*. 1996). Open folds and brittle faults affecting the Miocene molasse of Bas-Dauphiné also implies WNW-ESE to E-W compression (Blès & Gros 1991). Such mild Late Miocene compression, also affecting most of the Massif Central, would be a far-field effect of the Alpine collision (Blés *et al*. 1989; Blès & Gros 1991, and references therein). At the end of the Miocene, between 7.7 and 6.4 Ma effusive basaltic volcanism produced lava flows that reached Rochemaure less than 10 km north of Le Teil (Feraud 1979; Bandet *et al*. 1974, Fig. 1a). Contemporaneous dykes are mostly vertical and strike between N110 and N150 with a maximum between N135° and N150° and are compatible with a compression of that direction (Feraud & Campredon 1983).

Post-Pliocene normal faults imply an E-W to NE-SW extension in Bas-Dauphiné that would result from a transcurrent state of stress with sigma 1 trending N-S to NW-SE and sigma 3 trending E-W to NE-SW (Blès & Gros 1991). Because the southern part of the CFS has a clear geomorphic trace and offsets left-laterally valleys and Quaternary terraces, it has been interpreted to be active with an average slip rate of 0.1–2 mm yr^{-1} (Lacassin *et al*. 1998a). Such conclusion is controversial and has stirred up intense scientific discussion (Ambert *et al*. 1998; Mattauer *et al*. 1998; Sébrier *et al*. 1998; Lacassin *et al*. 1998b). The Nîmes fault, located ∼40 km to the SE, shares nearly the same trend and is considered as active (Grelet *et al*. 1993; Sébrier *et al*. 1997). While the palaeo-seismic record is very sparse in France, a palaeoearthquake was identified on the Nîmes fault in Courthézon, 50 km south of Le Teil, associated with reverse offsets on a ∼N50 oriented fault (Carbon *et al*. 1993). The most recent synthesis of active faults in France considers the Nimes fault as a Quaternary fault and the Alès basin border fault, as well as segments of the Pontet-de-Couloubre and Marsanne faults, as potentially active (Fig. 1; Jomard *et al*. 2017).

The SISFRANCE database on historical seismicity (sisfrance.net) reveals several earthquake swarms in 1773, 1873 and 1933–1936, with maximum associated intensities of VII, 20 km SW of Le Teil (Cornou *et al*. 2021). Yet, one of the 1873 shocks could be located as close as 5 km south of Le Teil. The BCSF-RéNaSS catalogue (renass.unistra.fr) contains only one earthquake with a magnitude over 4, and two between 3 and 4 at less than 60 km from Le Teil in the last decades (since 1981 March 03; Delouis *et al*. 2019). In 1923, an M_w 3 earthquake is located at Le Teil (Manchuel *et al*. 2018). More recently in 2002–2003, a very shallow (< 200 m) earthquake swarm (M_L < 2) was detected in the Tricastin area, 20 km SW of Le Teil (Thouvenot *et al*. 2009).

Present-day strain rates estimated by GNSS over the last 10 yr are of 1 ± 0.4 nanostrain per year with a compression trending ∼N110, translating into ∼0.1 mm yr^{-1} of shortening over a 100 km long transect (Delouis *et al*. 2019; Masson *et al*. 2019, Fig. 1a). *In situ* stress measurement in Boussenac, 36 km north of Le Teil, indicates a N140 maximum horizontal compression (Fig. 1a, Heidbach *et al*. 2018).

As a summary, the Le Teil area is located in a continental intraplate zone where present deformation is slow, but not negligible, and where numerous faults are present. The most preeminent ones strike NE-SW, dip to the SE and are inherited from an Oligocene phase of extension.

3 GEOLOGICAL 3-D MODEL

In order to discuss potential relationships between the geological structure and the earthquake rupture, we build a 3-D geological model of a 7 × 10 km area surrounding the surface rupture and the epicentre to a depth of 3 km below sea level. The surface geology of le Teil area was already described on geological maps of Aubenas (Kerrien *et al*. 1989) and Montélimar (Lorenchet *et al*. 1979) at the scale of 1:50 000, as well as on the harmonized map of Ardèche (Saint Martin 2009). However, the design of a 3-D geological model requires new fieldwork and the re-definition of geological units.

3.1 Methods

We build a 3-D geological model using the GeoModeller software. In such a model, layer orientations measured in the field are interpolated to define a potential field that describes the geometry of the corresponding formation (Lajaunie *et al*. 1997; Calcagno *et al*. 2008). The base of each formation is an isopotential surface that goes through contact point(s) relative to the underlying formation. The formations parallel to each other are grouped into series. A geometrical relationship must be defined for each series (erosive or onlapping) depending on whether it crosscuts the underlying ones or not (Calcagno *et al*. 2008). This approach is well adapted to model the geometry of sedimentary series but requires the definition of the series and having as many structural measurements (orientations of the layers) and contact points as possible. Faults are considered as discontinuities in the potential fields. They are defined by their own potential-field, from orientation and location data, and can be set as infinite if they are continuous across the whole model, or finite if they end within the model box. It is necessary to define which formations and other faults are cut by each fault.

3.2 Stratigraphic pile

Most formations outcropping in the model zone are Lower Cretaceous marine sediments including limestones, marls and marl-limestones alternations. The so-called Urgonian facies (Barremian, lower-Aptian), ubiquitous in the Vocontian basin, corresponds to a more than 200 m thick layer of massive light limestones that are exploited by the cement industry (which includes a historical Lafarge site, active since 1833, and a large active quarry still in operation). Overlying layers are mainly silico-clastic, with sandstones, marls and calcareous sandstones of Upper Aptian, Albian, Cenomanian and Turonian age. That transition is due to a progressive emersion, considered as a far-field effect of the Pyrenean orogenesis, but it is not associated with a major angular unconformity. A main stratigraphic unconformity is present at the base of the Oligocene continental deposits (conglomerates and coloured sands).

The model stratigraphic pile is built from the stratigraphy described in detail for the 1:50 000 Aubenas geological map (Elmi *et al*. 1996), taking into account the 3-D model specificities. Superficial, mostly Quaternary, deposits are not described in the 3-D model. According to the geological map, 16 other formations outcrop in the zone. Whilst all these formations have been identified in the field, some of them were merged and only 8 formations appear in the model pile (Fig. 2 and Fig. S1, Supporting Information). Underlying formations do not outcrop in the restricted zone at the surface but appear in the model as 5 distinct formations (Fig. 2 and Fig. S1, Supporting Information). Names given to the new formations do not reflect precise stratigraphic ages. Despite some sedimentation

gaps and slight unconformities, all Mesozoic formations have been gathered in the same series, while the Oligocene corresponds to a discordant series.

3.3 Fieldwork

During 10 d of fieldwork, we collected data at more than 300 locations (Fig. 2b). We used these data to build a geological database aimed at standardizing the storage, referencing, and sharing of geological data. Most of these data consists in the determination of the facies and in their attribution to the stratigraphic chart and formations of the 3-D model pile, as well as measurements of the strike and dip of the stratification (Fig. S2, Supporting Information). Other data are defined as contact points at the base of a series or as fault location (Fig. S2, Supporting Information).

One key point of 3-D geological modelling is to define the fault network. In the Le Teil area, because of the dense vegetation cover, most faults are defined from the mapping of the sedimentary formations, but some faults may be directly observed in the field. The LRF was already mapped previously (Kerrien *et al*. 1989), and we carefully checked its trace along which fault planes are exposed at four locations (e.g. Fig. 3a). While the main fault trace trends N50 on average, local fault planes trend from N5 to N80. Observations of slickensides on fault planes suggest that the more easterly trending planes have a large strike-slip component (Fig. 3b). The LRF have locally a clear geomorphic expression (Ritz *et al*. 2020), and we were able to precisely map its trace between the outcropping planes on a LiDAR Digital Elevation Model (DEM) acquired one week after the earthquake, with a resolution of 25 cm (same data used by Ritz *et al*. 2020). Both this trace and fault plane measurements collected on the field constrain the geometry of the LRF in the 3-D model.

About 2 km west of Le Teil, the Pontet-de-Couloubre fault and the Valgayette fault are 200 m apart from each other and bound the Rochemaure Oligocene basin (Fig. 2b). The two faults merge further north. Several other NNW-SSE (∼N150) strike-slip faults, unreported in previous mapping, are visible in the field, including spectacular fault planes (Fig. 3c and Figs S3b and S4, Supporting Information). Our fault mapping is mostly in agreement with the existing geological maps. Differences arise as only the main faults appear in the 3-D model. We also slightly changed the trace of some of them and found some unreported faults (Fig. 2). The main faults in the 3-D model are NE-SW striking, SE dipping normal faults crossing the whole zone, affecting both the Cretaceous and Oligocene deposits: *Alba*, *Pontet-de-Couloubre* (that was previously considered as two distinct faults: Pontet-de-Couloubre and Saint-Thomé faults), *Valgayette* (with a different trace), *La Rouvière* and *Bayne-St-Alban* faults (Fig. 2). Three other finite faults, as they do not cross the whole area, are also considered in our 3-D model: the Rocherenard fault (shorter and subdivided in two branches with respect to previous mapping), and two previously unreported faults trending N150 including the Violette fault (VF).

3.4 Other constraints

We used 15 strike and dip measurements from the Ardèche geological map (Saint Martin 2009), at locations that we could not explore (Fig. 2b and Fig. S2, Supporting Information), to complement our field data. As the 3-D geological model does not assume any formation thickness, it is necessary to dispose of contact points for the formations that do not outcrop. For this purpose, we used the interpreted log of the Valvignère (VAL 1) 4600 m deep borehole (Fig. S5, Supporting Information, http://infoterre.brgm.fr/page/banque-sol-bss). Although this borehole is located 1 km outside the model box (Fig. 1b), the stratification is almost flat in this area. Therefore, we could safely translate it within the box at a location with similar elevation and outcropping formation (Fig. S2, Supporting Information).

As the data set remains heterogeneous, with for example few data in the eastern part of the model because of the Quaternary sediments cover in the Rhône valley or in the Le Teil urban area, and with very few constraints at depth, the initial GeoModeller solution barely manages to fit all surface observations. It is thereby necessary to add additional constraints to the model. The methodology is somewhat the same as that followed by a geologist drawing cross-sections at depth from information limited to the surface, making some basic assumptions, such as the continuity of the layers (in the absence of faults) and the approximate conservation of their thicknesses. We hence define *ad-hoc* additional constraints to the model. The resulting geological map reproduces most of the surface observations (Fig. 2b), with some discrepancies considered as negligible. It is worth noting that the 3-D geometry of the faults at depth is only defined from field-based measurements.

3.5 Results

The resulting 3-D geological model is provided in a 3-D PDF format in Supporting Information, while 3-D views in Fig. S6 (Supporting Information), and 2-D views of the model are shown in Figs 2(b) and (c) and Fig. S7 (Supporting Information). The surface map shows the same general pattern as the previous geological maps (Kerrien *et al*. 1989; Saint Martin 2009), with the same major faults and the Bayne and Rochemaure syncline folds (Fig. 2 and Fig. S7, Supporting Information). However, they differ by several points. (1) The existing maps show necessarily more complexity and details than our simplified model. (2) We locally have different interpretations regarding the fault network. For instance, on previous maps, the northern part of the LRF fault is cut by four, possibly dextral, NW-SE faults. We did not detect such faults and, based on the LiDAR DEM and field work, we assume that the fault is continuous. In the same area, we map the Rocherenard fault as discontinuous and not connected to LRF to the NE. Conversely, we add in the 3-D model two finite faults with a N150 azimuth, because we have clear field evidence of their importance in the local structure (Fig. 3c and Fig. S4, Supporting Information). We interpret these faults as dextral faults linked to the N-S Pyrenean compression phase. (3) Consistent with our field observations, the two syncline folds limbs have significantly lower dips than those depicted on previous geological maps (Fig. S7, Supporting Information). However, their fold axes are compatible with a post-Oligocene NW-SE compression, associated with the 'Rhodanian' deformation phase according to Elmi *et al*. (1996). At other locations we observed folds with axes compatible with that deformation phase (Fig. 3d). These structures are too small to be visible in the 3-D model, but out of our mapping zone (South of Bayne syncline), two large NE-SW anticlines are described by Elmi *et al*. (1996).

The geological 3-D model allows us to estimate apparent normal offsets of ∼1000 and ≥ 150 m for the Pontet-de-Couloubre-Valgayette and Bayne-St-Alban, respectively. The offset on the LRF ranges between 100 and 200 m.

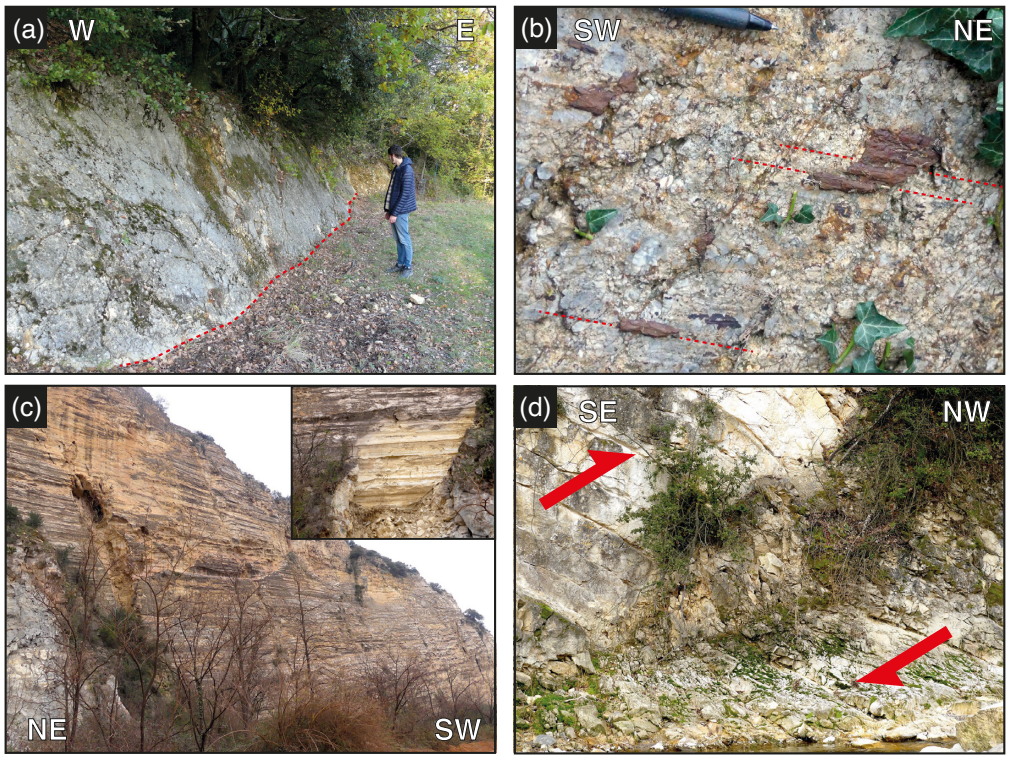

Figure 3. Field observations. (a) *[Site LT11]* Fault plane striking N45-60° E attributed to LRF. Neither clear slickensides nor evidence of recent coseismic slip was found on this plane, although it appears collocated with the InSAR-derived rupture (within its location's uncertainties). (b) *[Site LT5b]* Slickensides (N80-22°) on the LRF fault plane striking N73-72° S. (c) *[Site LT122]* 200 m long, >30 m high fault plane striking N150, delimiting an abandoned quarry face in Le Teil cement quarry. This plane displays well-marked slickensides close to horizontal (inset: closer view). (d) *[Site LT106]* Knee-bend, close to faulting, with a horizontal fold axis trending ∼N55. This compression evidence could be associated with the recent Alpine tectonic phase responsible for the Le Teil earthquake. Locations of sites 3a to 3d are shown on Fig. 2.

4 InSAR TIME-SERIES ANALYSIS

The coseismic interferograms produced in the days following the Le Teil earthquake played a key role in guiding the early post-seismic field missions in the earthquake area (Delouis *et al*. 2019; Cornou *et al*. 2021). This data set helped to constrain the location and spatial extent of the surface rupture, guiding further seismological, geodetic and tectonic studies of the earthquake (Mordret *et al*. 2020; Ritz *et al*. 2020; De Novellis 2020; Causse *et al*. 2021; Vallage *et al*. 2021).

However, past studies of the earthquake involving InSAR data rely on the analysis of only a limited number of individual coseismic interferograms. All were computed from radar images acquired by the ESA's Sentinel-1 satellites a few days before and after the earthquake (Cornou *et al*. 2021; Ritz *et al*. 2020; De Novellis 2020, Vallage *et al*. 2021). These interferograms were processed and unwrapped using different methodologies and remain affected by atmospheric phase delays and coherence loss. Here we use a time-series analysis of Sentinel-1 data acquired every 6 d over a period of about ten months before the earthquake and three months after the earthquake. This approach aims (1) to improve the signal-to-noise ratio and refine the coseismic surface displacement field (Grandin *et al*. 2017; Liu *et al*. 2021), in particular the surface slip distribution along fault, by mitigating stratified tropospheric phase delays and averaging temporally uncorrelated atmospheric noise (see Section 4.1), and (2), given the shallow depth of the earthquake, to investigate potential shallow deformation along the fault during the pre- and post-seismic periods.

4.1 Data and methods

We derive a time-series of surface displacement from Sentinel-1 images acquired in Interferometric Wide Swath mode along one ascending track (relative orbit A059, Table 1). We use the complete data archive between 2019 January 04 and 2020 January 29, from subswath IW3 only (incidence angle of ∼44°), cropped in an 80 by 80 km zone around the earthquake epicentre (Fig. 1a). We follow a Small Baseline Subset (SBAS) approach to take advantage of the redundancy on the phase information in a network of interferograms in order to compensate for temporal decorrelation and atmospheric delays (Berardino *et al*. 2002). Our network of interferograms (Fig. S8, Supporting Information) includes both short and long temporal baselines, with a maximum time span of 11 months, resulting in 254 interferograms built from 66 images.

The interferogram processing and time-series inversion are performed using the NSBAS software (Doin *et al*. 2011), partly derived from ROI_PAC (Rosen *et al*. 2004) and adapted to Sentinel-1 data for spectral diversity corrections (Grandin 2015). Orbital and topographic corrections are performed using ESA precise orbits and the Shuttle Radar Topography Mission (SRTM) 1-arcsec DEM (Farr *et al*. 2007). Corrections from stratified tropospheric phase delays are computed using the ERA5 reanalysis data from the European Centre for Medium-Range Weather Forecast (ECMWF, Doin *et al*. 2009; Jolivet *et al*. 2011). Interferograms are multilooked by a factor of 4 in azimuth and 16 in range for unwrapping, leading to a final pixel size of about 80 m. Filtering is made through a weighted average of the phase gradient, based on colinearity (Pinel-Puyssegur *et al*.

Table 1. InSAR data set used as input for the slip inversion.

Sentinel-1 track	Type of data	Acquisition dates	Final downsampling distance (m)
A059 (ascending)	Coseismic displacement extracted from the time-series	Between 2019-01-04 and 2020-01-22	200
A161 (ascending)	Interferogram	2019/11/01–2019/11/13	400
D037 (descending)	Interferogram	2019/11/11–2019/11/17	400
D139 (descending)	Interferogram	2019/11/06–2019/11/12	400

2012), in sliding windows of 6 pixels. Unwrapping is performed using the branch-cut algorithm (Goldstein *et al*. 1988). The coherence threshold used to build masks before unwrapping is adapted depending on the temporal baseline of the interferograms, and on whether the interferogram contains coseismic signal or not. We set the unwrapping to be more restrictive for the long temporal baseline interferograms than for the short baseline ones, in order to avoid unwrapping errors due to temporal decorrelation. For the coseismic interferograms only, a manual cut is also introduced to prevent the unwrapping path from crossing the rupture. The trace of this manual cut (Fig. 4) is both consistent with the phase discontinuity visible on the wrapped unfiltered interferograms, with the main surface ruptures we observed on the field, and with the LRF inherited scarp revealed by the LiDAR high-resolution DEM (Ritz *et al*. 2020). Unwrapped interferograms are first visually checked in order to detect large unwrapping errors.

We iteratively compute the time-series to recover the phase evolution at each date of acquisition from the unwrapped differential interferograms. Considering a typical SBAS approach, the phase delays of unwrapped interferograms are inverted pixel by pixel to solve for the total phase delay of each date relative to the first date. We apply an additional linear constraint in case subnetworks of interferograms for a pixel could not be connected due to unwrapping issues (López-Quiroz *et al*. 2009). After a first inversion, we remove the noisiest interferograms from the data set as well as those presenting large scale unwrapping errors, using a root mean square (RMS) misclosure criterion (pixelwise misclosure within the interferogram network after time-series inversion, López-Quiroz *et al*. 2009). The network thus reduces to 199 interferograms based on 60 images (Fig. S8, Supporting Information). Residual unwrapping errors are automatically corrected in an iterative procedure during the final NSBAS time-series computation, using network adjustment to minimize the RMS misclosure (see RMS misclosure averaged per pixel in Fig. S9a, Supporting Information).

In the following analysis, we mask pixels that are not covered by at least one coseismic interferogram. Indeed, some pixels close to the rupture zone are not necessarily unwrapped on coseismic interferograms due to decorrelation. As the time-series inversion is performed for each pixel independently, if a pixel has not been unwrapped in any coseismic interferogram, the pre- and post-event interferograms' subnetworks are disjoint for this pixel. In that case, the algorithm extrapolates the pre-event linear trend to the post-event period (López-Quiroz *et al*. 2009), leading to potentially incorrect coseismic displacement values at these pixels.

In a last step, we perform a temporal decomposition of the unfiltered time-series to extract the coseismic displacement (similarly to Grandin *et al*. 2017) as well as a linear velocity. The LOS displacement at a given pixel d_{LOS} at a time t writes as:

$$d_{\mathrm{LOS}}(t) = a.t + b.H(t_{\mathrm{cos}}) + c \quad (1)$$

where a is the velocity, b the coseismic offset, H a Heaviside step function, t_{cos} the date of the earthquake and c an offset parameter to account for atmospheric noise in the first image of the time-series (used as reference). We do not include a seasonal term in this decomposition as the relatively short time span of the time-series (one year) does not provide enough information to constrain it well. Finally, maps of ground velocity, coseismic displacement and cumulative residual of the decomposition are geocoded for further analysis.

4.2 Results

The coseismic line of sight (LOS) displacement map (Fig. 4a) displays less noise than single interferograms for the same track, thanks to the time-series analysis procedure described above. This coseismic map shows an excellent spatial coverage on the NW side of the earthquake rupture (footwall), while higher decorrelation on the hangingwall leads to slightly worse coverage on the SE side. In the LOS, we observe up to 10 cm of positive displacement (toward satellite) on the hangingwall and 7 cm of negative motion on the footwall (away from satellite), with a maximum relative displacement reaching 16 cm in the SW part of the rupture, close to the location 4.65° E, 44.52° N (Figs 4a and d). Other smaller local slip maxima can be noticed in the NE part of the rupture. Our results confirm that the total rupture length is about 5 km (Fig. 4d).

The green squares in Fig. 4(d) indicate the vertical offsets measured by Ritz *et al*. (2020) using terrestrial LiDAR, projected in the LOS, so that they are comparable to our InSAR relative displacements (black profile in Fig. 4d), assuming that the displacements measured by InSAR are mainly in the vertical direction. Surface displacements measured by LiDAR at sites numbers 1, 2 and 7 are much smaller than the total amount of displacement retrieved by InSAR. This inconsistency is most likely explained by a difference of scale and resolution between the techniques used, since InSAR measures the distributed deformation (at tens of metre scale) while field LiDAR measures more localized deformation (at centimetre scale). This would be consistent with the suggestion by Ritz *et al*. (2020) that the deformation is more distributed in the northeastern segment of the rupture. On the contrary, LiDAR measurement number 5 indicates a slightly larger displacement than the one estimated by InSAR. This might be explained by the 500 m distance between our two profiles. If the deformation is very localized in this part of the rupture, as suggested by Ritz *et al*. (2020), the relative displacement between these two InSAR profiles may not capture the maximum of the displacement because they are not close enough to the fault. Therefore, the field measurement could exceed the InSAR measurement there.

The linear velocity of the time-series decomposition is difficult to interpret (Fig. 4b). Given the very low compression rate in the Le Teil region (∼0.1 mm yr^{-1} in the ∼N110 direction, Masson *et al*.

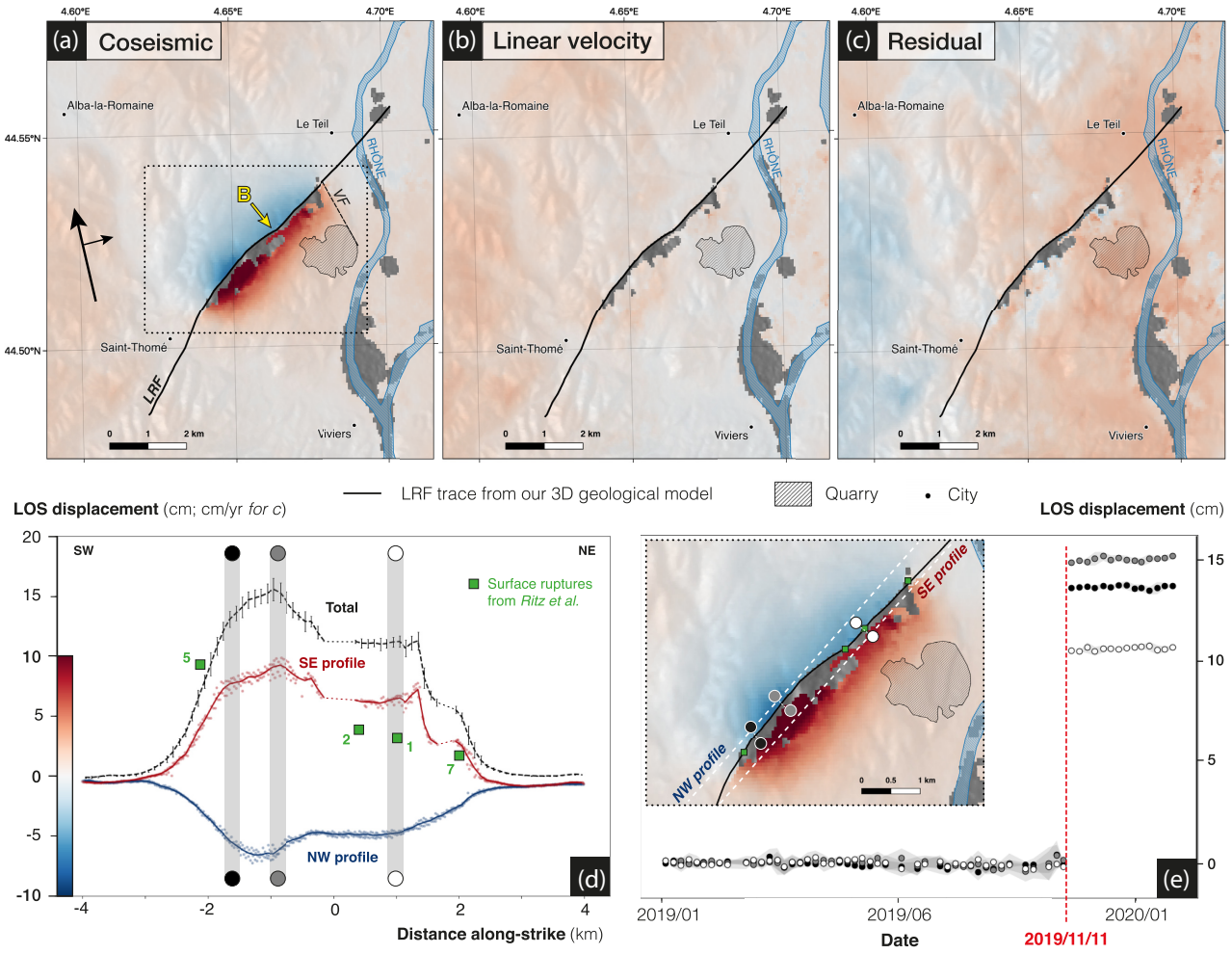

Figure 4. InSAR time-series decomposition results (a) Coseismic LOS displacement and (b) linear LOS velocity, best-fitting the InSAR time-series over the entire observation time span. (c) Cumulative residual displacement of the InSAR time-series decomposition, after removing coseismic signal and cumulative displacement due to linear trend. (d) Along-strike distribution of coseismic LOS displacement. Red (respectively, blue) profile shows slip distribution along the southeastern (respectively, northwestern) side of the fault; see location of profiles in (e). Black profile is the differential between red and blue profiles and represents the total relative displacement along the rupture trace (error bars correspond to the sum of the standard deviations of the two profiles). Green squares are vertical surface displacements (projected on LOS) measured by terrestrial LiDAR from Ritz *et al.* (2020), with their original numbering. Grey vertical bars indicate along-strike location of sites for which InSAR time-series are shown in (e). (e) Relative time-series for three pairs of points located on each side of the rupture (black, grey, white dots located on inset map from (a). 2 sigma envelope of noise level is shown in light grey. Colour code for InSAR maps in (a) to (c) and (e) is shown on vertical axis of d (*in cm for a, c, e; in cm* yr^{-1} *for b*). Positive LOS changes indicate motion toward the satellite. The yellow 'B' in a indicates a fault bend discussed in Section 6.2. *LRF:* La Rouvière Fault and *VF:* Violette Fault.

2019), this linear term most likely represents the aliased seasonal atmospheric signal, dominating, especially as our time-series covers a relatively short time span (one year).

After removing the coseismic and linear trend from the unfiltered time-series, we analyse the cumulative residual displacement map to detect potential pre-seismic deformation or afterslip. We do not identify (Fig. 4c) any clear spatial pattern in the vicinity of the LRF that could be interpreted as pre- or post-earthquake deformation. The cumulative displacement map from post-seismic dates only does not show such pattern either. Thus, we conclude that there was no post-seismic deformation for this earthquake, or at least no *detectable* post-seismic deformation (it might be too small or too deep to be seen with InSAR). It justifies the simple decomposition strategy adopted, into linear and coseismic terms only, without a post-seismic logarithmic term. The analysis of the relative LOS displacement between points located on either side of the Le Teil earthquake rupture only a few hundred metres from each other confirms no relative pre- or post-seismic motion (Fig. 4e). Such a relative displacement between points situated at very close distance can be assumed to be little affected by atmospheric noise because spatially correlated noise is largely removed by the double-difference operation. No obvious signal arises in the relative time-series associated with these points, although it shows a higher dispersion from 2019 May to the date of the earthquake (0.29 and 0.48 cm before and after May, respectively). However, due to the short time span covered and the lack of a specific spatial pattern near the fault, we interpret this higher dispersion as a residual uncorrelated seasonal signal, possibly of atmospheric or hydrological origin, rather than actual pre-seismic deformation.

5 COSEISMIC SLIP INVERSION

We rely on InSAR data as the only geodetic data available to invert for the coseismic slip distribution at depth, using the CSI python

library (github.com/jolivetr/csi; Jolivet *et al*. 2015). We use as input the LOS coseismic displacement map extracted from our time-series as described in Section 4 for track A059, and unwrapped coseismic interferograms for the other three tracks (Table 1 and Fig. S11, Supporting Information). These single interferograms were processed following the same workflow and parametrization as described in Section 4.1, except for the multilooking factors, which are 2 in azimuth and 8 in range for unwrapping, leading to a final pixel spacing of about 40 m.

We downsample the four InSAR data sets using a distance-based algorithm in CSI (pixel size decreases as an exponential function of the distance to the fault trace). As we have more confidence in the displacement map derived from our time-series, especially in the near-field, we downsample this data set using a final 200 m resolution (closest to the fault) while using 400 m for interferograms. This leads to a greater number of data points (about 1100), and therefore a greater weight in the inversion for track A059 than for the other three tracks (about 470 data points each). In order to prevent some of the downsampled pixels to cut across the surface trace of the fault, we remove all points within a 180 m buffer in the vicinity of the fault trace. Our data set still preserves a high level of detail on the near-fault deformation signal enhanced by the time-series, helping to constrain the shallow part of the slip distribution.

We model surface displacements due to slip on dislocations embedded in a homogeneous elastic half-space. Our fault model is tied to the surface trace of the LRF defined in our 3-D geological model derived from field observations and LiDAR analysis and projected onto the free surface of the elastic half-space. From this trace, striking N43 in average, we build a fault plane with a constant dip (the value of which is detailed hereafter) to the southeast, discretized into triangular patches. The patch size is ∼150 m at the surface, increasing to ∼300 m at the base of the fault (at a depth of around 4 km). We compute the Green's functions relating unit slip on each triangular patch to surface displacements using the method of Meade (2007) for triangular patches. We perform a static inversion using a non-negative least-squares strategy (Tarantola 2005), with the regularization scheme of Radiguet *et al*. (2011). We account for uncertainties in the InSAR data through the calculation of a data covariance matrix describing the spatial correlation of the pixels (Lohman & Simons 2005; Sudhaus & Jónsson 2009; Jolivet *et al*. 2014, 2015).

With this setting, we explore the influence of fault dip on the slip distribution for fault planes with dips ranging between 30° and 75°. We compare the different models using a posterior log-likelihood (LLK) function quantifying the misfit associated with each fault geometry (a low LLK indicates smaller misfit). Considering the four InSAR tracks the LLK curves show that a dip between 55° and 60° is favoured by the data, (Fig. 5a). This range is consistent with the dips measured on LRF fault planes on the field with an average fault plane striking N44-69° SE (Fig. 5c). We use a fixed dip of 57° for the final inversion.

We then explore the regularization parameters of the inversion, introduced through a model covariance matrix. Three parameters are used in the regularization (Radiguet *et al*. 2011; Maubant *et al*. 2020): σ_m a damping value and λ the correlation length, relative to a scaling factor λ_0, fixed at the minimum interpatch distance (150 m). We optimize the values of σ_m and λ through L-curves analysis (Fig. S10, Supporting Information), by choosing the best compromise between model roughness (quantified by maximum slip) and the misfit to the data (Radiguet *et al*. 2011). We use the values $\sigma_m = 0.7$ and $\lambda = 2.5$ km for the final inversion.

The LOS surface displacements predicted by our preferred slip model match well the InSAR data (Fig. S11, Supporting Information), with RMS of residual displacements ranging between 0.18 and 0.51 cm. Consistently with its overweighting in the inversion process, the displacement field on track A059 is especially well reproduced with a 0.43 cm RMS misfit (Fig. 6d). Our model slightly overestimates the coseismic LOS displacement in the hangingwall (Fig. 5b). After testing several faults dips, we conclude that such feature cannot be fitted with a constant dip geometry, as suggested by the ∼5° range of equivalent probability dips in Fig 5(a). Our model though is the best compromise for optimizing the fit to LOS displacement for each track and on both sides of the fault.

The resulting slip distribution inverted for the Le Teil earthquake has an equivalent moment magnitude of 4.9, consistent with seismological estimates (Delouis *et al*. 2019; Cornou *et al*. 2021; Vallage *et al*. 2021). The scalar seismic moments are 3.11×10^{16} and 0.9×10^{16} N·m for dip-slip and strike-slip, respectively, showing a dominating reverse dip-slip motion (Figs 6a and b). This is consistent with the surface InSAR data (Fig. S11, Supporting Information) displaying a dominance of the vertical motion in the hangingwall (displacement toward satellite for both looking angles) and a dominance of fault-perpendicular horizontal motion in the footwall with respect to vertical motion (opposite signs of motion on ascending and descending tracks). The dip-slip distribution along the fault is characterized by two areas of larger slip: a large one in the SW part of the fault with a maximum slip of 30 cm at 500 m depth and a smaller one in the NE part of the rupture with a maximum dip slip of 24 cm at similar depth. Displacements modelled at the surface have lower amplitudes, with a maximum dip-slip component of 23 cm on the shallowest patches (Fig. 6a). The slip profiles along depth (top left inset in Fig. 6a) highlight this shallow slip deficit reaching 23 per cent of the maximum slip, which will be discussed later.

We performed extensive testing on the strike-slip component of the slip model, which produced very variable distributions and senses of slip. Together with the high dependency of the strike-slip distribution to the setting of the inverse problem (non-negative least-square inversion versus bounded inversion for example), this suggests that the strike-slip component is poorly constrained by our data set. While the best-fitting model that we present here includes a minor (< 9 cm, Fig. S12, Supporting Information) left-lateral component, we estimate we cannot trust either its distribution, or the sense of the strike-slip motion, and do not discuss them further.

To qualitatively assess the robustness of our slip model along fault strike and depth, we compute the sensitivity of the inversion (Loveless & Meade 2011, Fig. 6c and Fig. S12b, Supporting Information). Note that sensitivity is a purely qualitative indicator (the absolute values actually depend on the number of data we use in the inversion). Only Bayesian approaches could provide a meaningful confidence interval to the estimated slip values. For the dip-slip component, despite small shallow variations due to lack of data close to the fault, sensitivity only decreases significantly below 2 km depth where slip vanishes. We therefore state that our modelled dip-slip distribution is correctly constrained by the data above that depth. Note that the sensitivity for the strike-slip component appears on average about one order of magnitude lower than the dip-slip one (Fig. S12b, Supporting Information).

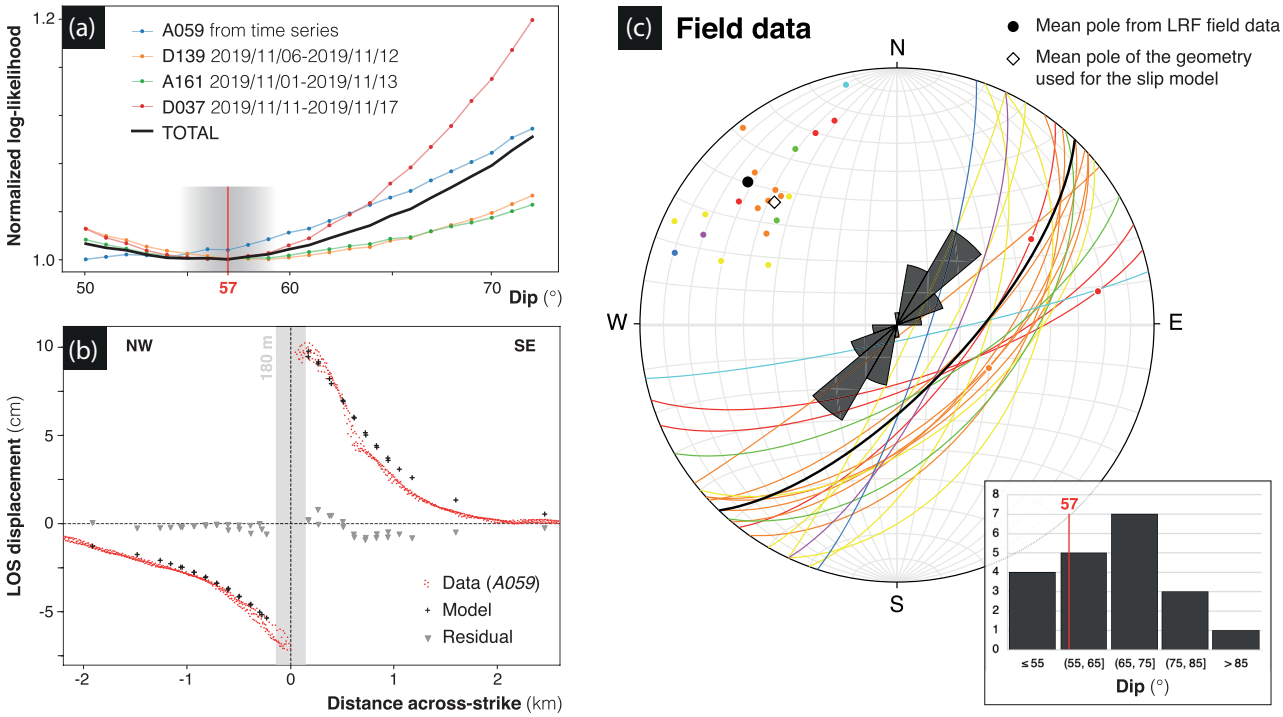

Figure 5. Dip exploration from InSAR analysis and comparison with field data for LRF. (a) Dip exploration for InSAR data inversion, based on normalized LLK function. Colours represent different tests made using single coseismic interferograms or coseismic slip map extracted from time-series analysis (Fig. 4a). Black curve shows the average function for the whole data set, with best-fitting dips in the range 54°–59° and a minimum misfit for 57°. (b) Fault-perpendicular LOS coseismic displacement profile (located in Fig. 6d) for A059 track extracted from time-series analysis (red dots), compared with corresponding final model profile (black crosses), and model versus data residuals (grey triangles). Data within 180 m from the fault were discarded in the inversion (see the text for details). (c) Field observations of LRF planes, shown in a stereonet (equal area, lower hemisphere projection). Each colour corresponds to an outcrop. The mean LRF pole (solid black circle; N314-21°) and plane (black line) are computed from averaging individual poles and planes of each outcrop. The circles located on lines represent slickenside measurements. The pole of the average fault geometry used for slip inversion from InSAR data (white diamond; N315-33°) is shown for comparison. Inset shows dip distribution of the LRF planes measured on the field, compared to the 57° value chosen for the final InSAR data inversion.

6 DISCUSSION

6.1 Reactivation of LRF and rupture geometry

Our results, combining 3-D geological mapping, InSAR time-series analysis and slip inversion suggest a reactivation of the LRF during the 2019 Le Teil earthquake. The trace of the LRF defined in our 3-D geological model is compatible with the rupture displayed by the InSAR signal. Moreover, although no direct evidence of reactivation was found on the LRF planes, the main evidence of surface rupture associated with the Le Teil earthquake (on which vertical offset could be measured by Ritz *et al*. 2020) are located very precisely on our trace of LRF (Fig. S13, Supporting Information). Other evidence was found within several tens to hundreds of metres from the LRF trace, but were less probably directly related to the rupture (e.g. gravitational collapse). Our slip model using a geometry based on the LRF fault trace is able to reproduce InSAR data with a very good level of agreement, reinforcing the consistency of the reactivation hypothesis.

Thanks to a time-series approach, we improve the coverage of the displacement field extracted from InSAR, compared to interferograms produced just after the earthquake and used in published studies. We show the absence of pre-event deformation or afterslip, while providing, for one Sentinel-1 track, an accurate coseismic LOS displacement map. Although our unwrapping approach is more conservative than in some other works (De Novellis *et al*. 2020; Ritz *et al*. 2020), we ensure we can trust all our unwrapped displacements, especially for the highly decorrelating zone in the SW neighbourhood of the rupture. Doing so, we limit the risk of overinterpreting the data.

It should be noted that the InSAR displacement map from our time-series does not show a multisegmented rupture, contrary to what has been suggested so far (De Novellis *et al*. 2020; Ritz *et al*. 2020). Instead, our data favour a single rupture trace, collocated with the LRF trace. We compared the previously published rupture traces with our coseismic displacement map (Fig. S13, Supporting Information). The trace from De Novellis *et al*. (2020) appears to be inconsistent with our data, (1) as their main segment is too straight and does not follow the InSAR discontinuity, and (2) as our displacement map does not display any evidence for a secondary rupture along La Chade fault. The rupture trace from Ritz *et al*. (2020) generally follows the surface trace of the LRF that we infer. However, our data are not consistent with secondary ruptures in the NE part of the hangingwall. As the secondary ruptures presented in these two studies are not mutually consistent, we speculate that inconsistencies mainly stem from noise in in the coseismic interferograms they used, which are mitigated in our time-series analysis.

Additionally, our study brings additional constraints on the LRF dip, both at the surface and at depth. Field measurements of LRF planes yield a mean strike of N44 and dip of 70° to the SE (Fig. 5c), however associated with a large dispersion (95 per cent confidence

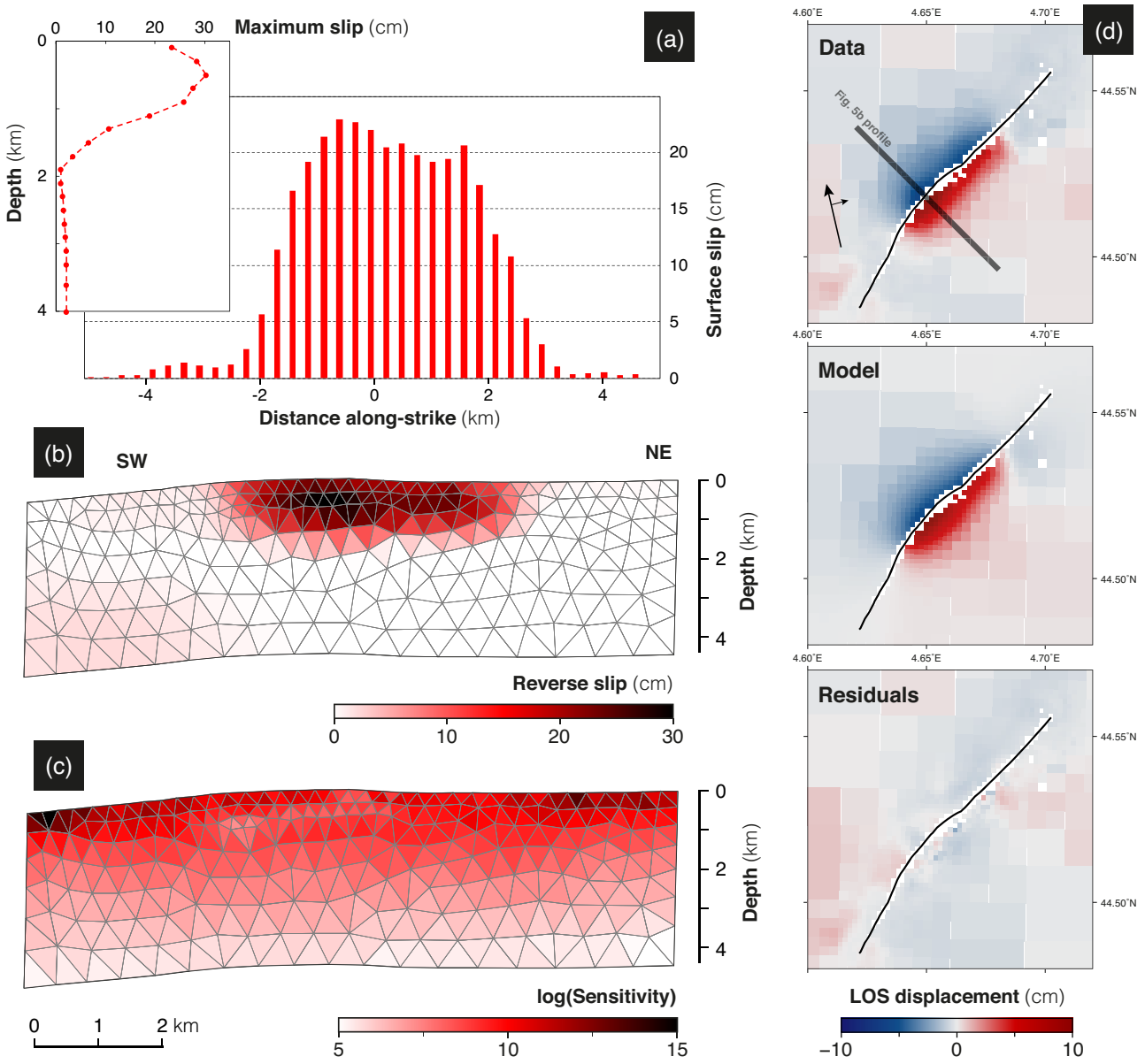

Figure 6. Best slip model. (a) Along-strike distribution of surface slip in our final slip model (dip-slip component only). Inset shows depth distribution of maximum slip. (b) Slip distribution for dip-slip component (strike-slip is shown in Fig. S6, Supporting Information). (c) Sensitivity (Loveless & Meade 2011) of the inversion for the dip-slip component (see Fig. S12 in the Supporting Information for the strike-slip one). (d) Top: downsampled data from time-series analysis of A059 track, used for slip inversion; middle: model and bottom: residuals.

interval about ± 17°). The inversion of the InSAR data reveals a best-fitting dip in the range 55°–60° (Fig. 5a). Considering the uncertainty on these estimates, we argue that the LRF should not show substantial variations of dip angle in the depth range ruptured by the Le Teil earthquake (< 2 km), although we cannot exclude a slight steepening close to the surface. De Novellis *et al.* (2020) used a 52° dip on the LRF for their two faults slip model, and a 62° dip for their single fault geometry, consistent with our modelling results. Vallage *et al.* (2021) find best-fitting dips for a single fault of 60° using InSAR, still in agreement with our estimates. Regarding seismological estimations of the focal mechanism, Vallage *et al.* (2021) propose a nodal plane striking N45-65° SE, while Delouis *et al.* (2021) propose nodal planes striking N45 to N65 and dipping 40 to 60° E from waveform inversion. They are all consistent with our results and also suggest that the LRF has a similar dip from the surface to at least 1–1.5 km depth, where the earthquake likely nucleated.

6.2 Potential interactions between 3-D geology, fault geometry and earthquake slip

The implementation of a local 3-D geological model, combined with the slip model derived from InSAR offers the opportunity to study potential interactions between the earthquake slip and the pre-existing 3-D geological structure. The more recent relocations of the point source of the Le Teil earthquake by Delouis *et al.* (2021)

can be discussed together with our slip distribution. The epicentral area that they estimate is located between the western part of Le Teil quarry and the LRF (Figs 1a and 2b), with a source depth between 1 and 2 km (Figs 2c and 7; Delouis *et al*. 2021). It is consistent with our estimate of the fault location and dip.

Our fieldwork allows us to map a previously unknown fault, displaying post-Cretaceous strike-slip motion (Fig. 3c), with a N150 orientation, that we named VF. In the field, we found no evidence of any fault north of its inferred crossing point with the LRF. We therefore map the VF fault stopping on the LRF fault, assuming that the LRF is more recent. Our InSAR coseismic displacement map shows that the uplift of the hangingwall vanishes to the NE in the area where the VF intersects the LRF (Fig. 4a). Consistently, our modelled slip on fault tapers down to zero to the NE in the interaction zone between the VF and LRF (Fig. 7c). We speculate that the connection area of the two faults could have acted as a barrier to the north-eastward propagation of the earthquake, as already documented for other cases in literature (e.g. Klinger *et al*. 2006; Walters *et al*. 2018).

The combination of our 3-D geological model and the slip model also allows one to study potential geological constraints on the depth extension of slip during the earthquake. As mentioned earlier, the Le Teil earthquake is very shallow, and slip does not exceed 25 per cent of its maximum value (i.e. slip $<$ 8 cm) at depths larger than 1.5 km (Fig. 6a). Our 3-D geological model shows a lithological transition at $\sim$1 km depth ($\pm$ 100 m between the footwall and the hangingwall of the LRF) between massive limestone units (n3e-f) on the top and an underlying thick ($\sim$1 km) marl unit (n3a-d) (Figs 7b and c). This transition is likely associated with a downdip drop of rock rigidity along the LRF plane. This feature was previously noticed in local velocity models (Causse *et al*. 2021), by the need to introduce a low-velocity zone about 1 km thick at depths greater than 1200 m. Earthquake propagation is known to be facilitated in high rigidity media. Specifically, in a region where geological units are similar to those observed in Le Teil region, Gratier *et al*. (2013) showed that limestones' layers favour seismic slip while marls often creep. Thus, our results suggest that while most of slip occurred in massive limestones (n3e-f and n4b-c, i.e. the Urgonian limestones), the n3a-d marls layer could have prevented the earthquake nucleation and/or propagation at greater depth.

According to our slip model, the coseismic slip reached the surface along the whole rupture length ($\sim$5 km), but with heterogeneous amounts of surface slip. Two main slip maxima can be identified in the surface slip distribution (Figs 6a and 7a), corresponding to the two main slip patches of the slip distribution at depth. A significative change in the LRF strike, marked by a peak at N60, is observed in between these two maximum slip locations and is marked 'B' in Figs 4(a) and 7(a) and (b). This change in azimuth is well resolved since the central portion of the LRF was mapped using a 25-cm LiDAR DEM and complemented by field measurements (while the SW and NE parts of the LRF—greyish in Fig. 7(a)—were only constrained by a few outcrops). Such type of geometrical complexity may act as barrier to earthquake rupture propagation (King & Nabelek 1985; Wesnousky 2006; Klinger *et al*. 2006). Hence, we suggest that this change in the LRF surface geometry could have restrained the slip propagation. We have no constraints on the potential downdip continuation of this relay zone. However, considering the shallowness of the slip distribution, its impact could remain significant at depth, and maybe have contributed to the delimitation of the two slip maxima.

6.3 A singular earthquake

The characteristics of this earthquake make it out of range in the Wells & Coppersmith (1994) empirical relationships. According to these scaling laws, a 5 km surface rupture length is usually associated with an M_w 5.8–6.1 event, and a 30 cm maximum displacement should result in an M_w 6.3–6.5 earthquake. The Le Teil earthquake does not fit either the updated relationships from Leonard (2010) between rupture length and seismic moment. However, these relationships are not necessarily suited for very small and shallow events, for which small-scale variations of physical parameters of the crust could play a critical role (e.g. 2010 M_w 4.9 Pisayambo earthquake, Champenois *et al*. 2017).

The shallow slip deficit displayed by our model is also present in the InSAR-derived slip models from previous studies (Delouis *et al*. 2019; De Novellis *et al*. 2020; Vallage *et al*. 2021). In the framework of a homogeneous elastic half-space inversion, it is difficult to assess whether Surface Slip Deficit (Fialko *et al*. 2005) is a real feature or an artifact resulting from the lack of data coverage close to the fault, or caused by neglecting the likely complexities of the elastic medium (Xu *et al*. 2016; Marchandon *et al*. 2021). Slip modelling is probably more sensitive to these parameters for such a small event than for larger events, for which the spatial resolution is often decreased for the sake of computational tractability. Taking advantage of the 3-D geological model built in this study to create a layered 2-D, or even 3-D, elastic model, and use it to compute the Green's functions, although technically feasible, is beyond the scope of the present study. This would require a way to quantify the physical parameters of the rocks from the different geological facies we observed in the field. This could be achieved through lab experiments on samples or the comparison of the 3-D geology with a local velocity model derived from seismological observations. A good resolution in the very shallow part (depth $<$ 500 m) of such an elastic model would be needed to improve tangibly the fit of the surface displacements.

The Le Teil earthquake occurred on an ancient normal fault, for which we observe no evidence of post-Oligocene activity. As suggested by Ritz *et al*. (2020), although the LRF has a clear geomorphic expression, it is not sharp enough to result from a significant seismic activity in the last tens of thousands of years. An ongoing work by Ritz *et al*. (2021) suggests from palaeoseismological trenches that the LRF could have hosted at least one event in the historical period, with kinematic features consistent with reverse motion. Pending the outcome of these palaeoseismological results to come up, based only on geomorphology, we cannot know how recent the first reactivation of the LRF as reverse fault since Oligocene is, as the very slow deformation relative to the erosion rates likely hinders the preservation of this recent activity.

Why this earthquake occurred on the LRF, when it is not the fault displaying the largest cumulative offset in the area according to our 3-D geological model, is still a matter to debate. Actually, fieldwork and 3-D geological modelling have not given us any argument to explain the occurrence of an earthquake on the LRF rather than on any other. The very shallow depth of the event and the small number of aftershocks (Cornou *et al*. 2021), coupled with the presence of a large active quarry in the LRF hangingwall have led some to propose that the earthquake was induced by a reduction of normal stress along the LRF due to the artificial discharge (De Novellis *et al*. 2020). This hypothesis has led to a national and international public media debate raising major issues of liability and seismic risk. It has been discussed by a national scientific commission (Delouis *et al*. 2019) and scientific publications (Ampuero *et al*. 2020; De Novellis *et al*. 2020), but no definite answer has yet been reached. Our

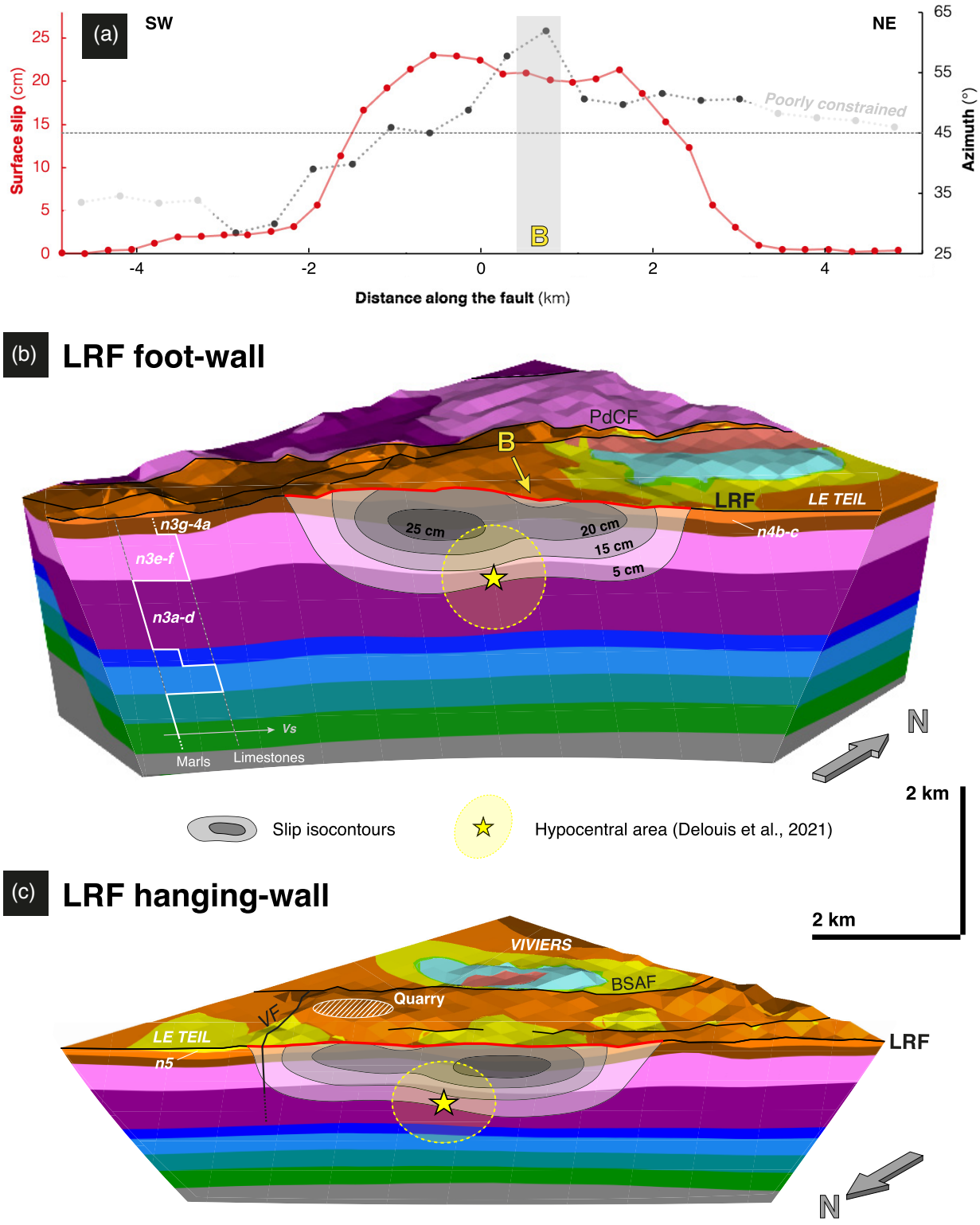

Figure 7. 3-D summary of Le Teil earthquake rupture characteristics. (a) Along-strike coseismic surface slip distribution derived from our model (in red, dip-slip component only) compared to along-strike variations of local fault azimuth (in grey). Poorly constrained azimuths due to limited LRF field evidences are plotted in lighter grey. The yellow 'B' letter shows the main bend mentioned in the text. (b) and (c) 3-D views of the NW (b) and SE (c) part of our 3-D geological model, cut along the LRF fault plane. The detailed lithological description is in Fig. 2. A qualitative velocity model, assumed to represent the variability of rigidities of rocks observed in the field is plotted in (b) (left-hand side). The isocontours of the slip distribution inferred from InSAR are superimposed in grey, together with hypocentral area (in yellow) from seismological data (preferred relocation of the main shock by Delouis *et al*. 2021, with associated uncertainty of ∼500 m). *PdCF:* Pontet-de-Couloubre-Fault; *LFR:* La Rouvière Fault; *VF:* Violette Fault and *BSAF:* Bayne-St-Alban Fault.

study did not focus on this aspect, and we found no element which could help in the debate. InSAR time-series shows no localized deformation that could be associated with the quarry discharge. Tracking such a signal, if it exists, would probably necessitate to study a much longer InSAR time-series.

The geological and structural framework in which the 2019 Le Teil event occurred, characterized by NE-SW oriented faults cutting limestones and marls units, is quite ubiquitous along the right-bank of the Rhône river between latitudes 44.3 and 44.8° N (Fig. 1a). Moreover, many other smaller quarries exploit the Urgonian limestones in this region. The assessment of the seismic potential of the many faults similar to the LRF, potentially in relation with quarrying activities, is of paramount importance, given the presence of two nuclear power plants located 15 km north and 25 km south of Le Teil. Future studies combining 3-D geology, subsurface imaging and palaeo-seismology should help improve the knowledge of faults' activity in this slowly deforming region. Furthermore, the integration of geological data sets at regional scale, together with seismological observations could benefit to seismic hazard assessment, for example through the identification of geological units associated with a higher probability of seismic slip (such as the Urgonian limestone layer, e.g. Thouvenot *et al*. 2009).

7 CONCLUSION

The 2019 M_w 4.9 Le Teil earthquake, while not causing heavy fatality, reveals a critical lack of knowledge regarding the activity of the northeastern part of the CFS, emphasized by a high vulnerability due to the proximity to nuclear facilities and populated areas.

Our study helps characterize the Le Teil earthquake through a multidisciplinary approach. The 3-D geological modelling that we carried out provides an updated view of the local geological and structural context in which this event occurred. Our InSAR work enhances the coseismic displacement map proposed previously from single interferograms, and rules out the existence of a significant deformation in the 10 months before and 3 months after the event. The inversion of InSAR data for slip distribution reveals the consistency between InSAR observations and the modelled 3-D geometry of the Oligocene LRF. The slip model shows almost purely reverse faulting along a single ∼5 km long rupture, with two main slip patches reaching 30 cm and 24 cm of slip, respectively, at 500m depth, and a fault dip of 55°–60°. The rupture ends at the intersection between the LRF and the previously unmapped VF which may have acted as a barrier. Our analysis also suggests that both a fault bend and rigidity contrasts in the local stratigraphy influenced the slip distribution. These results confirm that the area is currently undergoing a WNW-ESE shortening which, whilst slow, could reactivate older faults inducing damaging seismicity, and therefore calls for a reassessment of the seismic hazard.

ACKNOWLEDGEMENTS

This work has been supported by the CNRS-INSU and LGL-TPE. RJ has received funding from the European Research Council (ERC) under the European Union's Horizon 2020 Research and Innovation Programme (grant agreement: 758210—Geo4D) and from the Institut Universitaire de France. We acknowledge the constructive reviews of two anonymous reviewers and the Editor H. Yao.

DATA AVAILABILITY

Sentinel-1 data are available online through PEPS (https://peps.cnes.fr) or Copernicus (https://scihub.copernicus.eu) platforms. Precise orbits were downloaded from European Space Agency's Sentinel-1 website (https://qc.sentinel1.eo.esa.int/, in March 2020). SRTM data are provided on Earthdata portal (https://earthdata.nasa.gov). ECMWF ERA5 data are available at https://ecmwf.int.

The database of geological observations (DataGeol) generated during this study is available at https://zenodo.org/record/4836308#.YLDijDYzYWp.
The principal maps extracted from the InSAR time-series analysis can be downloaded at https://zenodo.org/record/4836335#.YLDokS8isWo.

AUTHORS CONTRIBUTION

PHL and CL conceived the study. LM and PHL did fieldwork. LM and SC did geological 3-D modelling. LM and CL processed and analysed the InSAR time-series. LM, RJ and CL carried inversion of slip distribution. RG and OC contributed to InSAR processing. LA provided the LiDAR data and contributed to its analysis. LM, PHL, CL, RJ, RG and MM contributed to the interpretation and discussion of the results, and writing the manuscript.

REFERENCES

Ambert, P., Philip, H. & Ritz, J., 1998. Commentaires à la note de R. Lacassin, B. Meyer, L. Benedetti, R. Armijo et P. Tapponnier. 'Signature morphologique de l'activite de la faille des Cevennes (Languedoc, France)', *C. R. Acad. Sci. Ser. IIA,* **12,** 857–859.

Ampuero, J.-P. *et al.,* 2020. The November 11 2019 Le Teil, France M5 earthquake: a triggered event in nuclear country, *Presented at the EGU General Assembly 2020,* EGU. doi:10.5194/egusphere-egu2020-18295.

Arène, J., Berger, G., Gras, H., Poidevin, J. & Sauvel, C., 1978. Carte géologique de la France au 1/50000, feuille Alès (912) Bureau de Recherches Géologiques et Minières

Arthaud, F. & Laurent, P., 1995. Contraintes, déformation et déplacement dans l'avant-pays Nord-pyrénéen du Languedoc méditerranéen, *Geod. Acta,* **8,** 142–157.

Arthaud, F. & Matte, Ph., 1975. Les décrochements tardi-hercyniens du sud-ouest de l'europe. Géometrie et essai de reconstitution des conditions de la déformation, *Tectonophysics,* **25,** 139–171.

Arthaud, F. & Seguret, M., 1981. Les structures pyreneennes du Languedoc et du Golfe du Lion (Sud de la France), *Bull. Soc. Géol. France,* **S7-XXIII,** 51–63.

Bandet, Y., Donville, B. & Gourinard, Y., 1974. Premières datations potassium argon du Coiron (Ardèche, France), *C.R. de l'Académie des Sciences de Paris,* **279,** 2869–2872.

Barbarand, J., Lucazeau, F., Pagel, M. & Séranne, M., 2001. Burial and exhumation history of the south-eastern Massif Central (France) constrained by apatite fission-track thermochronology, *Tectonophysics,* **335,** 275–290.

Berardino, P., Fornaro, G., Lanari, R. & Sansosti, E., 2002. A new algorithm for surface deformation monitoring based on small baseline differential SAR interferograms, *IEEE Trans. Geosci. Remote Sensing,* **40,** 2375–2383.

Bergerat, F & Martin, P., 1993. Mise en évidence d'une tectonique distensive synsédimentaire et caractérisation du champ de contraintes au Trias inférieur-moyen sur la bordure vivaro-cévenole du Bassin du Sud-Est de la France: la région de Largentière et le forage Balazuc-1 (programme Géologie Profonde de la France), *C. R. Acad. Sci. Sér. 2,* **316,** 1279–1286.

Bergerat, F. & Martin, P., 1994. Analyse des failles du forage Balazuc-1 (programme GPF) et reconstitution des paleo-états de contrainte sur la bordure vivaro-cévenole du bassin du sud-est de la France; relations avec la marge europeenne de la Tethys ligure, *Bull. Soc. Géol. France,* **165,** 307–315.

Bergerat, Françoise., 1987. Stress fields in the European platform at the time of Africa-Eurasia collision, *Tectonics,* **6,** 99–132.

Blés, J.L., Bonijoly, D., Castaing, C. & Gros, Y., 1989. Successive post-Variscan stress fields in the French Massif Central and its borders (Western European plate): comparison with geodynamic data, *Tectonophysics,* **169,** 79–111.

Blès, J.L. & Gros, Y., 1991. Stress field changes in the Rhone Valley from the Miocene to the present, *Tectonophysics,* **194,** 265–277.

Bodeur, Y., 1976. Evaluation de l'amplitude du décrochement cévenol par le décalage des facies récifaux portlandiens des environs de Ganges (Hérault), *C. R. Acad. Sci. Paris*.**282** 961–963

Bonijoly, D., Perrin, J., Roure, F., Bergerat, F., Courel, L., Elmi, S. & Mignot, A., 1996. The Ardèche palaeomargin of the South-East Basin of France: mesozoic evolution of a part of the Tethyan continental margin (Géologie Profonde de la France programme), *Mar. Pet. Geol.,* **13,** 607–623.

Calcagno, P., Chilès, J.P., Courrioux, G. & Guillen, A., 2008. Geological modelling from field data and geological knowledge, *Phys. Earth planet. Inter.,* **171,** 147–157.

Carbon, D., Combres, P., Cushing, M. & Granier, T., 1993. Enregistrement d'un paléoséisme dans des sédiments du pléistocene supérieur dans la vallée du Rhône: quantification de la déformation, *Géol. Alpine,* **69,** 33–48.

Causse, M., Cornou, C., Maufroy, E., Grasso, J.-R., Baillet, L. & El Haber, E., 2021. Exceptional ground motion during the shallow Mw 4.9 2019 Le Teil earthquake, France, *Commun. Earth Environ,* **2,** 14p. doi:10.1038/s43247-020-00089-0.

Champenois, J. *et al.,* 2017. Evidences of surface rupture associated with a low-magnitude (Mw 5.0) shallow earthquake in the Ecuadorian Andes, *J. geophys. Res. Solid Earth,* **122,** 8446–8458.

Chantraine, J., Autran, A. & Cavelier, C.,, Carte Géologique de la France au 1/1000000 (6e édition) Bureau de Recherches Géologiques et Minières 1996.

Chardon, D., Aretz, M. & Roques, D., 2020. Reappraisal of Variscan tectonics in the southern French Massif Central, *Tectonophysics,* **787,** 228477.

Choi, J.-H., *et al.,* 2018. Geologic inheritance and earthquake rupture processes: the 1905 M $\geq$ 8 Tsetserleg-Bulnay strike-slip Earthquake Sequence, Mongolia, *J. geophys. Res. Solid Earth,* **123,** 1925–1953.

Cornou, C., *et al.,* 2021. Rapid response to the M w 4.9 earthquake of November 11, 2019 in Le Teil, Lower Rhône Valley, France, *C. R.. Géosci.,* **353,** 1–23.

De Novellis, V., Convertito, V., Valkaniotis, S., Casu, F., Lanari, R., Monterroso Tobar, M.F. & Pino, N.A., 2020. Coincident locations of rupture nucleation during the 2019 Le Teil earthquake, France and maximum stress change from local cement quarrying, *Commun. Earth Environ.,* **1,** 20p. doi:10.1038/s43247-020-00021-6.

Delouis, B. *et al.* Rapport d'évaluation du groupe de travail (GT) CNRS-INSU sur le séisme du Teil du 11 novembre 2019 et ses causes possibles (in french), CNRS-INSU. 11 Décembr,e 2019. http://www.cnrs.fr/sites/default/files/press_info/2019-12/Rapport_GT_Teil_phase1_final_171219_v3.pdf.

Delouis, B., Oral, E., Menager, M., Ampuero, J.-P., Guilhem Trilla, A., Régnier, M. & Deschamps, A., 2021. Constraining the point source parameters of the 11 November 2019 Mw 4.9 Le Teil earthquake using multiple relocation approaches, first motion and full waveform inversions, *C. R. Géosci.,* **353,** 1–24.

Deville, E., Blanc, E., Tardy, M., Beck, C., Cousin, M. & Ménard, G., 1994. Thrust Propagation and Syntectonic Sedimentation in the Savoy Tertiary Molasse Basin, *Hydrocarbon and Petroleum Geology of France ed. Mascle, A., Berlin, Heidelberg: Springer Berlin Heidelberg,* 269–280, doi:10.1007/978-3-642-78849-9_19.

Dèzes, P., Schmid, S.M. & Ziegler, P.A., 2004. Evolution of the European Cenozoic Rift System: interaction of the Alpine and Pyrenean orogens with their foreland lithosphere, *Tectonophysics,* **389,** 1–33.

Doin, M.-P., Guillaso, S., Jolivet, R., Lasserre, C., Lodge, F., Ducret, G. & Grandin, R., 2011. Presentation of the small baseline NSBAS processing chain on a case example: the Etna deformation monitoring from 2003 to 2010 using Envisat data, pp. 3434–3437, *Presented at the Proceedings of the Fringe symposium,* ESA SP-697 Frascati, Italy.

Doin, M.-P., Lasserre, C., Peltzer, G., Cavalié, O. & Doubre, C., 2009. Corrections of stratified tropospheric delays in SAR interferometry: validation with global atmospheric models, *J. appl. Geophys.,* **69,** 35–50.

Elmi, S. *et al.,* 1996. Notice explicative. Carte géologique de la France au 1/50000, feuille Aubenas (865),170p. , *Bureau de Recherches Géologiques et Minières*.

Elmi, S., 1983. La structure du Sud-Est de la France: une approche à partir de la bordure vivaro-cévenole du Massif Central, *C. R. Acad. Sci.—Ser. II,* **296** 1615–1620.

Farr, T.G. *et al.*, 2007. The Shuttle Radar Topography Mission, *Rev. Geophys.,* **45,**(2), doi:10.1029/2005RG000183.

Feraud, G., 1979. Age et mise en place du volcanisme du massif du Coiron (Ardèche, France), *C. R. Acad. Sci. Paris,* **289**.1005–1008

Feraud, Gilbert & Campredon, R., 1983. Geochronological and structural study of tertiary and quaternary dikes in southern france and sardinia: an example of the utilization of dike swarms as paleostress indicators, *Tectonophysics,* **98,** 297–325.

Fialko, Y., Sandwell, D., Simons, M. & Rosen, P., 2005. Three-dimensional deformation caused by the Bam, Iran, earthquake and the origin of shallow slip deficit, *Nature,* **435,** 295–299.

Ford, M. & Lickorish, W.H., 2004. Foreland basin evolution around the western Alpine Arc, *Geol. Soc., Lond., Spec. Publ.,* **221,** 39–63.

Gautheron, C., Tassan-Got, L., Barbarand, J. & Pagel, M., 2009. Effect of alpha-damage annealing on apatite (U–Th)/He thermochronology, *Chem. Geol.,* **266,** 157–170.

Goldstein, R.M., Zebker, H.A. & Werner, C.L., 1988. Satellite radar interferometry: two-dimensional phase unwrapping, *Radio Sci.*, **23,** 713–720.

Grandin, R., 2015. Interferometric processing of SLC Sentinel-1 TOPS data, in *Presented at the FRINGE'15: Advances in the Science and Applications of SAR Interferometry and Sentinel-1 InSAR Workshop,* ESA, Frascati, Italy, 23-27 March 2015.

Grandin, R., Vallée, M. & Lacassin, R., 2017. Rupture process of the Mw5.8 Pawnee, Oklahoma, Earthquake from Sentinel-1 InSAR and seismological data, *Seismol. Res. Lett.,* **88,** 994–1004.

Gratier, J.-P., Thouvenot, F., Jenatton, L., Tourette, A., Doan, M.-L. & Renard, F., 2013. Geological control of the partitioning between seismic and aseismic sliding behaviours in active faults: evidence from the Western Alps, France, *Tectonophysics,* **600,** 226–242.

Grellet, B., Combes, P. & Granier, T., 1993. *Sismotectonique de la France métropolitaine dans son cadre géologique et géophysique: avec atlas de 23 cartes au 1/4 000 000ème et une carte au 1/1 000 000ème* Société géologique de France

Heidbach, O. *et al.,* 2018. The World Stress Map database release 2016: crustal stress pattern across scales, *Tectonophysics,* **744,** 484–498.

Illies, J.H., 1972. The Rhine graben rift system-plate tectonics and transform faulting, *Geophys. Surv.,* **1,** 27–60.

Jolivet, R. *et al.,* 2014. The 2013 Mw 7.7 Balochistan Earthquake: seismic potential of an accretionary wedge, *Bull. seism. Soc. Am.,* **104,** 1020–1030.

Jolivet, R., Grandin, R., Lasserre, C., Doin, M.-P. & Peltzer, G., 2011. Systematic InSAR tropospheric phase delay corrections from global meteorological reanalysis data: correcting InSAR with ERA-Interim, *Geophys. Res. Lett.,* **38,** n/a-n/a. doi:10.1029/2011GL048757.

Jolivet, R., Simons, M., Agram, P.S., Duputel, Z. & Shen, Z.-K., 2015. Aseismic slip and seismogenic coupling along the central San Andreas Fault, *Geophys. Res. Lett.,* **42,** 297–306.

Jomard, H., Cushing, E.M., Palumbo, L., Baize, S., David, C. & Chartier, T., 2017. Transposing an active fault database into a seismic hazard fault model for nuclear facilities – Part 1: building a database of potentially active faults (BDFA) for metropolitan France, *Nat. Hazards Earth Syst. Sci.,* **17,** 1573–1584.

Kalifi, A. *et al.,* 2021. Chronology of thrust propagation from an updated tectono-sedimentary framework of the Miocene molasse (western Alps), *Solid Earth Discuss.*, **2021,** 1–68, Copernicus Publications.

Kerrien, Y., Elmi, S., Busnardo, R., Camus, G., Kieffer, G., Moinereau, J. & Weisbrod, A., 1989. Carte géologique de la France au 1/50000, feuille Aubenas (865) Bureau de Recherches Géologiques et Minières

King, G. & Nabelek, J., 1985. Role of fault bends in the initiation and termination of earthquake rupture, *Science,* **228,** 984–987.

Klinger, Y., Michel, R. & King, G., 2006. Evidence for an earthquake barrier model from Mw∼7.8 Kokoxili (Tibet) earthquake slip-distribution, *Earth planet. Sci. Lett.,* **242,** 354–364.

Lacassin, R., Meyer, B., Benedetti, L., Armijo, R. & Tapponnier, P., 1998a. Geomorphic evidence for Quaternary sinistral slip on the Cévennes Fault (Languedoc, France), *C. R. Acad. Sci. Ser. IIA,* **11,** 807–815.

Lacassin, R., Meyer, B., Benedetti, L., Armijo, R. & Tapponnier, P., 1998b. Réponse aux commentaires de Ambert et al., Mattauer et Sébrier et al. à la note: 'Signature morphologique de l'activité de la faille des Cévennes (Languedoc, France)', *C. R. Acad. Sci.—Ser. IIA,* **327,** 861–866, Elsevier Masson.

Lajaunie, C., Courrioux, G. & Manuel, L., 1997. Foliation fields and 3D cartography in geology: principles of a method based on potential interpolation, *Math. Geol,* **29,** 571–584.

Leonard, M., 2010. Earthquake fault scaling: self-consistent relating of rupture length, width, average displacement, and moment release, *Bull. seism. Soc. Am.,* **100,** 1971–1988.

Liu, F., Elliott, J.R., Craig, T.J., Hooper, A. & Wright, T.J., 2021. Improving the resolving power of InSAR for earthquakes using time series: a case study in Iran, *Geophys Res Lett,* **48**. doi:10.1029/2021GL093043.

Lohman, R.B. & Simons, M., 2005. Some thoughts on the use of InSAR data to constrain models of surface deformation: noise structure and data downsampling, *Geochem. Geophys. Geosyst.,* **6,** doi:10.1029/2004GC000841.

López-Quiroz, P., Doin, M.-P., Tupin, F., Briole, P. & Nicolas, J.-M., 2009. Time series analysis of Mexico City subsidence constrained by radar interferometry, *J. appl. Geophys.,* **69,** 1–15.

Lorenchet, D., Monjuvent, G., Bornad, M. & Combier, J., 1979. Carte géologique de la France au 1/50000, feuille Montélimar (866) Bureau de Recherches Géologiques et Minières

Loveless, J.P. & Meade, B.J., 2011. Spatial correlation of interseismic coupling and coseismic rupture extent of the 2011 Mw = 9.0 Tohoku-oki earthquake, *Geophys. Res. Lett.,* **38,**

Manchuel, K., Traversa, P., Baumont, D., Cara, M., Nayman, E. & Durouchoux, C., 2018. The French seismic CATalogue (FCAT-17), *Bull. Earthq. Eng.,* **16,** 2227–2251.

Marchandon, M., Hollingsworth, J. & Radiguet, M., 2021. Origin of the shallow slip deficit on a strike slip fault: influence of elastic structure, topography, data coverage, and noise, *Earth planet. Sci. Lett.,* **554,** 116696, doi:10.1016/j.epsl.2020.116696.

Martin, P. & Bergerat, F., 1996. Palaeo-stresses inferred from macro- and microfractures in the Balazuc-1 borehole (GPF programme). Contribution to the tectonic evolution of the Cévennes border of the SE Basin of France, *Mar. Pet. Geol.,* **13,** 671–684.

Masson, C., Mazzotti, S., Vernant, P. & Doerflinger, E., 2019. Extracting small deformation beyond individual station precision from dense Global Navigation Satellite System (GNSS) networks in France and western Europe, *Solid Earth,* **10,** 1905–1920.

Mattauer, M., Lacassin, R., Meyer, B., Benedetti, L., Armijo, R. & Tapponnier, P., 1998. Commentaires à la note de R. Lacassin, B. Meyer, L. Benedetti, R. Armijo et P. Tapponnier. 'Signature morphologique de l'activite de la faille des Cevennes (Languedoc, France)', *C. R. Acad. Sci. Ser. IIA,* **12,** 857–859.

Maubant, L. *et al.,* 2020. Independent component analysis and parametric approach for source separation in InSAR time series at regional scale: application to the 2017–2018 Slow Slip Event in Guerrero (Mexico), *J. geophys. Res. Solid Earth,* **125**. doi:10.1029/2019JB018187.

Meade, B.J., 2007. Algorithms for the calculation of exact displacements, strains, and stresses for triangular dislocation elements in a uniform elastic half space, *Comput. Geosci.,* **33,** 1064–1075.

Mordret, A. Brenguier, F. Causse, M. Boué, P. Voisin, C. Dumont, I. & Vernon, F.L. 2020. Seismic Stereometry Reveals Preparatory Behavior and Source Kinematics of Intermediate-Size Earthquakes, *Geophys. Res. Lett.,* **47**(17), doi.org/10.1029/2020GL088563.

Pinel-Puyssegur, B., Michel, R. & Avouac, J.-P., 2012. Multi-Link InSAR time series: enhancement of a wrapped interferometric database, *IEEE J. Sel. Top. Appl. Earth Observ. Remote Sensing,* **5,** 784–794.

Radiguet, M., Cotton, F., Vergnolle, M., Campillo, M., Valette, B., Kostoglodov, V. & Cotte, N., 2011. Spatial and temporal evolution of a long term slow slip event: the 2006 Guerrero Slow Slip Event: evolution of the 2006 Guerrero SSE, *Geophys. J. Int.,* **184,** 816–828.

Ritz, J.-F. *et al.,* 2021. Analyzing the paleoseismic history of the La Rouvière fault, unexpected source of the 11-11-2019, Mw4.9 Le Teil surface rupturing earthquake (Cévennes fault system, France), *Presented at the EGU General Assembly 2021, EGU,* doi:10.5194/egusphere-egu21-13044.

Ritz, J.-F., Baize, S., Ferry, M., Larroque, C., Audin, L., Delouis, B. & Mathot, E., 2020. Surface rupture and shallow fault reactivation during the 2019 Mw 4.9 Le Teil earthquake, France, *Commun. Earth Environ.*, **1,** 10p. doi:10.1038/s43247-020-0012-z.

Rosen, P.A., Hensley, S., Peltzer, G. & Simons, M., 2004. Updated repeat orbit interferometry package released, *Eos Trans. AGU,* **85,** 47–47.

Roure, F., Brun, J.-P., Colletta, B. & Van Den Driessche, J., 1992. Geometry and kinematics of extensional structures in the alpine foreland basin of southeastern France, *J. Struct. Geol.,* **14,** 503–519.

Roure, F., Brun, J.P., Colletta, B. & Vially, R., 1994. Multiphase extensional structures, fault reactivation, and petroleum plays in the Alpine Foreland Basin of Southeastern France, in *Hydrocarbon and Petroleum Geology of France*ed. Mascle, A., pp. 245–268, Berlin, Heidelberg: Springer Berlin Heidelberg. doi:10.1007/978-3-642-78849-9_18.

Saint Martin, M., 2009. Carte géologique harmonisée de l'Ardèche Bureau de Recherches Géologiques et Minières

Sanchis, E. & Séranne, M., 2000. Structural style and tectonic evolution of a polyphase extensional basin of the Gulf of Lion passive margin: the Tertiary Alès basin, southern France, *Tectonophysics,* **322,** 219–242.

Sébrier, M, Bellier, O., Peulvast, J. & Vergély, P., 1998. Commentaires à la note de R. Lacassin, B. Meyer, L. Benedetti, R. Armijo et P. Tapponnier. 'Signature morphologique de l'activite de la faille des Cevennes (Languedoc, France)', *C. R. Acad. Sci. Ser. IIA,* **12,** 855–856.

Sébrier, Michel, Ghafiri, A. & Bles, J.-L., 1997. Paleoseismicity in France: fault trench studies in a region of moderate seismicity, *J. Geodyn.,* **24,** 207–217.

Séranne, M., Benedicto, A., Labaum, P., Truffert, C. & Pascal, G., 1995. Structural style and evolution of the Gulf of Lion Oligo-Miocene rifting: role of the Pyrenean orogeny, *Mar. Pet. Geol.,* **12,** 809–820.

Soechting, W., 1996. *Etude et modélisation de la frac- turation de la partie septentrionale de la bordure viva- ro-cévenole autour de Privas (entre La Voulte-sur-Rhône et Aubenas),* Ardèche, Université Lyon 1.

Sudhaus, H. & Jónsson, S., 2009. Improved source modelling through combined use of InSAR and GPS under consideration of correlated data errors: application to the June 2000 Kleifarvatn earthquake, Iceland, *Geophys. J. Int.,* **176,** 389–404.

Tarantola, A., 2005. *Inverse Problem Theory and Methods for Model Parameter Estimation,* SIAM.

Thouvenot, F., Jenatton, L. & Gratier, J.-P., 2009. 200-m-deep earthquake swarm in Tricastin (lower Rhône Valley, France) accounts for noisy seismicity over past centuries, *Terra Nova,* **21,** 203–210.

Vallage, A. *et al.,* 2021. Multitechnology characterization of an unusual surface rupturing intraplate earthquake: the *M* L 5.4 2019 Le Teil event in France, *Geophys. J. Int.,* **226,** 803–813.

Walters, R.J. *et al.,* 2018. Dual control of fault intersections on stop-start rupture in the 2016 Central Italy seismic sequence, *Earth planet. Sci. Lett.,* **500,** 1–14.

Wells, D.L. & Coppersmith, K.J., 1994. New empirical relationships among magnitude, rupture length, rupture width, rupture area, and surface displacement, *Bull. seism. Soc. Am.,* **84,** 974–1002.

Wesnousky, S.G., 2006. Predicting the endpoints of earthquake ruptures, *Nature,* **444,** 358–360.

Xu, X. *et al.,* 2016. Refining the shallow slip deficit, *Geophys. J. Int.,* **204,** 1843–1862.

SUPPORTING INFORMATION

Supplementary data are available at *GJI* online.

Figure S1. Correspondence of stratigraphic logs between published geological maps, and our 3-D model, for units outcropping in the 3-D model zone.

Figure S2. Complete data set used as input for 3-D geological modelling.

Figure S3. Additional field observations. (a) *[Site LT123]* Thrust fault in barremian limestones, striking ∼N100 and offsetting a stratigraphic level by a few metres. (b) *[Site LT62]* Fault plane showing strike-slip slickensides in limestones. (c) *[Site LT59]* Shear zone oriented ∼N150 with C-S criteria suggesting a partially normal faulting. (d) *[Site LT29]* Normal fault in typical Oligocene coloured sands, with 17 cm offset. Sites' location is shown in Fig. S7 in the Supporting Information.

Figure S4. Stereonet of all fault field measurements. The ∼N150 strike-slip faults are in blue. All other faults measured are in red. Fig. 5(c) shows only the measurements corresponding to LRF.

Figure S5. VAL 1 borehole interpretation. The borehole is located at 4.5935° E, 44.4997° N.

Figure S6. 3-D view of the geological model. Colour code for units as in Fig. 2. (a) Complete view. (b) Truncated view to highlight LRF geometry.

Figure S7. Comparison of published and this study geological cross-sections. (a) Cross-section published in the Aubenas 1:50 000 geological map (Kerrien *et al*. 1989), located SW of the 3-D model zone. (b) Cross-section made from the standardized 1:50 000 geological map (Saint Martin 2009), across the 2019 Le Teil rupture on LRF. (c) Cross-section made from our 3-D geological model, along the same trace than (b). We refer to Aubenas geological map for stratigraphic description of a, stratigraphy of (b) and (c) is shown in Fig. S1 in the Supporting Information. *PdCF:* Pontet-de- Couloubre fault; *STF:* Saint-Thomé fault; *ValF:* Valgayette fault *LRF:* La Rouvière fault; *RF:* Rocherenard fault and *BSAF:* Bayne-St-Alban fault.

Figure S8. Relative perpendicular baseline as a function of time for SAR images (blue dots with reference image in red) and interferograms (black lines) network used in time-series analysis.

Figure S9. Uncertainties associated with the InSAR time-series. (a) RMS misclosure of the time-series inversion averaged per pixel. (b) and (c) Misfits from the temporal decomposition of the time-series, relative to the estimations of the coseismic step and the linear velocity, respectively.

Figure S10. Exploration of regularization parameters used in slip inversion (see the text for details).

Figure S11. Left (a) Downsampled coseismic InSAR displacement field (derived from time-series analysis on top or single interferograms at middle and bottom); centre (b) modelled surface displacement and right (c) residuals for best-fitting model.

Figure S12. Slip distribution and inversion sensitivity for strike-slip component.

Figure S13. Comparison of different rupture traces already published, from field or InSAR measurements: green squares, white dots and dashed blue lines from Ritz *et al*. (2020); yellow dashed line from DeNovellis *et al*. (2020); with the surface rupture trace used in this study (red line). Rupture traces superimposed (a) on satellite image (source) and LiDAR topographic map (source) and (b) coseismic displacement field from this study.

Please note: Oxford University Press is not responsible for the content or functionality of any supporting materials supplied by the authors. Any queries (other than missing material) should be directed to the corresponding author for the paper.